INVESTIGATION OF THE EFFECT OF HYDROGEL PORE MORPHOLOGY ON DNA MIGRATION MECHANISMS IN MICROCHIP GEL ELECTROPHORESIS

A Dissertation

by

NAN SHI

Submitted to the Office of Graduate and Professional Studies of
Texas A&M University
in partial fulfillment of the requirements for the degree of

DOCTOR OF PHILOSOPHY

Chair of Committee,	Victor M. Ugaz
Committee Members,	Zhengdong Cheng
	Tahir Cagin
	Jodie L. Lutkenhaus
Head of Department,	Nazmul M. Karim

December 2014

Major Subject: Chemical Engineering

ABSTRACT

Many efforts to develop advanced medical diagnostic capabilities rely on the ability to perform size-based separations of DNA and proteins. Miniaturized formats have potential to provide rapid integrated solutions, but rational development requires an improved understanding of the physics underlying separation. This dissertation majorly focuses on the DNA transport in microchip gel electrophoresis systems. We have developed a transport model that allows us to determine the interplay between the hydrogel pore size distribution, the applied electric field strength, and DNA size in determining separation performance. This fundamental understanding makes it possible to access a unique DNA transport mode, entropic trapping, that becomes dominant when the hydrogel pore size is close that of DNA coil. Further investigation of the entropic trapping phenomena, both experimentally and computationally, shows how the inherently disordered dynamics governing macromolecular transport under nanoconfined surroundings can paradoxically be precisely controlled. This capability lays a foundation for a sensitive probe of nanoscale molecular conformation, revealing previously unseen details about DNA-protein binding interactions at size scales far below the limits of conventional techniques. A key breakthrough is that our method is the first practical application of stochastic resonance in entropic trapping transport of macromolecules (previously studied, but only theoretically), yielding a new tool to "image" nanoscale details of biomolecular conformation.

ACKNOWLEDGEMENTS

I sincerely appreciate the great opportunity provided by Prof. Victor Ugaz, my academic advisor, to work in these interesting projects and numerous enlightening discussions that help me to find the right approaches. I am greatly thankful for your generous support that allows me to attend conferences worldwide and develop hobby projects. I also thank all my committee members for their great contributions including critical proofreading of my dissertation drafts. I also appreciate my lab mates for their help in my projects and great time we spent together watching the soccer games.

Of course I cannot make through this without the love and patience from my family members, especially my wife, Yichen Gao. Thank you so much for being with me during those difficult moments in my life.

TABLE OF CONTENTS

Page

LIST OF FIGURES

Page

LIST OF TABLES

Page

CHAPTER I

INTRODUCTION AND LITERATURE REVIEW

1.1 DNA Structures and Dynamics

Deoxyribonucleic acid (DNA) is an important type of biomolecule that contains genetic information used for used to regulate living activities. The molecular conformation of DNA can be either double stranded (dsDNA), consisting of two long-chain strands joined by hydrogen bonding to form the famous double helix structure, and single stranded (ssDNA), only composed one chain (half of the double-stranded helix). The molecular structure of DNA consists of a phosphate deoxyribose backbone with a series of nucleobases (guanine-G, adenine-A, thymine-T, cytosine-C) attached to the chain. In dsDNA, these necleobases form hydrogen bond between certain pairs, A-T and G-C, serve as stack force to stabilize the DNA's double helix structure (**Figure 1**).

DNA is viewed as a model polymer in many physics studies, and there are several key parameters associated with description. First, the distance along one base or one basepair is 0.34 nm that gives the *contour length*. The total length following the backbone is equal to this unit distance times the number of bases or basepairs in one chain. Another important parameter is the *Kuhn length*, which is a length scale above which the polymer could be considered as a series freely jointed segments. Since this parameter measures the stiffness of a polymer, dsDNA has a higher Kuhn length value of 100 nm compared with that of of ssDNA which is below 10 nm.

In order to simulate DNA behavior at realistic length and time scales, a coarse grained approach is generally adopted to model DNA as homopolymer consisting of a certain number of Kuhn segments N_k rather than tracking detailed interactions among all individual bases or basepairs (**Figure 2**). In free solution without external force, DNA molecule will take a random coil configuration, the size of which can be characterized by the *gyration radius* R_g. Considering a polymer with N freely jointed segments of statistical length a, one can arrive at following scaling $R_g \sim aN^{0.5}$ (de Gennes, 1979). To incorporate the interactions between segments (neglected in aforementioned gyration radius scaling), Flory (Flory, 1953) expressed the deviation from the ideal chain behavior in terms the *Flory exponent*, $R_g \sim aN^{\upsilon}$. In real 3D situations υ=0.58 that is larger than the exponent in ideal chain due to the interactions among segments.

Since the DNA backbone is phosphate-based, it will carry negative charges under common buffer conditions in the vicinity of pH 7. Therefore, DNA will experience an electrostatic force when an external electric field is applied, and its resulting motion in response to the force is quantified by a parameter called the *mobility* defined as the velocity divided by the strength of electric field, $\mu = v/E$. In free solution, this mobility is defined by the ratio of total charge carried by DNA over its drag coefficient, where both values are linearly related to DNA length in bases or basepairs. In other words, in free solution DNA of different length will move with the same mobility regardless of the value of electric field applied.

1.2 Electrophoresis and Separation of DNA in Gel Matrices

From the previous discussion, there appears to be a conundrum that it is impossible to separate DNA of different length in free solution (**Figure 3**). One way to overcome this barrier is to introduce a porous hydrogel matrix that will interact with DNA as it is travels through under the influence of the electrostatic driving force. Longer DNA will experience more interactions with the matrix that slow down its migration speed, introducing a size-dependent mobility that can be exploited to enable separations. Previous studies have identified two predominant transport regimes that can be accessed to separate DNA based on length by gel electrophoresis (Slater, Kenward, McCormick, & Gauthier, 2003). The first one is Ogston sieving (Ogston, 1958), where the free space within the matrix is much larger than the DNA size and DNA travels in its unperturbed form. In this regime, mobility is found to scale exponentially with the DNA fragment length. The second regime is called the reptation regime (Viovy, 2000) is encountered when the DNA size becomes much larger than the free space formed by the matrix. Here, molecular transport through the gel pores occurs via a snake-like motion along its contour and mobility scales inversely with the DNA length.

Recently (Liu, Li, & Asher, 1999; Rousseau, Drougin, & Slater, 1997; Smisek & Hoagland, 1990) a third intermediate regime has been shown to emerge that is of interest as a potential effective separation mechanism. This entropic trapping (ET) regime is encountered when the DNA size is comparable with the average size of free space in the gel matrix. A particularly intriguing observation about ET-dominated transport is that mobility becomes more strongly size dependent compared to the reptation regime. The

underlying transport phenomena has been revealed more recently using nanofabricated devices, where single DNA molecules could be directly observed to quantify the entropic penalty imposed by constrictions and the timescales associated with escape from this local energy trap.

1.3 New Emerging Microdevice Formats for Enhanced DNA Separations

As micromachining technologies become more mature, it is possible to fabricate very intricate microstructures capable of functioning as artificial gel matrices and develop novel separation techniques based on specific molecular interactions with these structures. For example, Dorfman's group (Ou, Cho, Olson, & Dorfman, 2009) fabricated a microchannel packed with isolated cylindrical posts. DNA molecules travelling through this post array will interact with these posts, experiencing several key events including initial collision, hook up around the post, and finally unhooking. The time scales of these interactions are related to DNA molecule length, so that different sized molecules will have different mobilities. Another example (Minc et al., 2005) utilizes self-assembly of superparamagnetic beads to form quasihexagonal post arrays. Other groups have (Craighead, Han, & Turner, 1999) successfully designed and fabricateed nanofilter architectures for DNA separation, where DNA molecules are driven by an electric field to migrate through a geometric path containing alternating deep wells and narrow slits . The depth of the narrow slit is close to sub Kuhn length scale of dsDNA and thus creates a low-entropy confining region for DNA molecules.

Despite successful demonstration of these novel separation principles, these previous attempts to exploit ET phenomena are usually are gel-free and involve complex nanofabrication processes. In our group, we have adopted an alternative approach to carry out DNA gel electrophoresis adapted to microchip format. The simple structure of the microchip allows routine fabrication, assembly and operations. Furthermore, in previous studies our group has developed a full protocol to facilitate automated operation and data collection of physical parameters associated with DNA transport. First, we choose photoinitiated polyacrylamide as our gel matrix so that we can precisely define the gel interface in the microchannel. We are also able to characterize the polyacrylamide gel pore morphology to provide crucial information about pore size distribution for the transport model discussed in Chapters III and IV. Second, the microchip format is precise and automated, allowing us to efficiently collect data needed to calculate mobility and diffusion coefficients simultaneously. These data are challenging to obtain in conventional macroscale slab gel systems.

1.4 Objectives and Outline

Despite increasing interest in DNA separations using microdevices, practical application of these systems is only possible after solving several critical issues. One problem is to ensure sufficiently high separation performance in limited length scales, which requires understanding of the interplay between gel structure, applied electric field, and separation resolution. Furthermore, to fully exploit the benefits of operating in the ET regime in hydrogel matrices, is necessary to explore this transport process in

detail. These studies are lacking primarily due to the difficulties in measuring transport parameters such as mobility and diffusion coefficients. The goal of our work is to obtain new information to understand how the nanoscale gel pore morphology influences the DNA transport mode in electrophoresis, and therefore the separation performance. With a special focus on the entropic trapping, we hope to fully explore its potential as new separation mechanism. Meanwhile, we utilize computational simulation techniques such as Brownian dyanmics and Monte Carlo simulation to investigate DNA migration dynamics in different environments that serve to provide more insight into possible DNA separation or manipulation techniques.

In Chapter II, details are presented about the experimental techniques employed, such as reagents, devices, and operational protocols. There is also brief introduction about the algorithms used for computer simulation.

In Chapter III a transport model is developed in order to quantify DNA migration behavior in gel matrices that is analogous to the structure of nanofilter. This model is used to construct a phase diagram of DNA transport mechanisms that incorporates various factors, such as the monomer and crosslinker concentration of the gel matrix, UV curing intensity, and applied electric field strength. Based on this diagram we are able to focus on the entropic trapping regime, which shows promising features for separations.

The intrinsically high diffusion encountered under entropic trapping transport is also revealed in Chapter III. Our effort to solve this problem is described in Chapter IV, where we introduce a pulsed electric field to globally synchronize the discrete hopping

events across the energy barrier. It enables us to increase separation resolution in the entropic trapping regime and yield interesting maximum mobility at a particular period of the pulsed electric field. The transport model developed in Chapter III is adapted to pulsed electric field operation to uncover the underlying stochastic resonance concept, allowing us to connect internal system events with observable parameters such as the period of electric field. A particularly interesting outcome is development of an entropic force microscope, demonstrating a convenient yet powerful approach to probe molecule structure based on observing the transport behavior while scanning the electric field over a range of actuation frequencies. This idea successfully detects different effects induced by YOYO-1 and daunomycin binding with DNA.

Chapters V and VII are dedicated to computational simulation of entropic trapping in various environments. Chapter VII is focused on the transport of Brownian particles in microchannels with alternating constrictions. By applying a periodic force we are able to achieve a stochastic resonance state where the particle's movement is synchronized with the shape function of the periodic force. This resonance state is very sensitive to the magnitude and frequency of the periodic force and therefore is helpful to design microfluidic systems for selective and stable trapping of particles. In Chapter VI we revisit the problem of long DNA transport in nanofilters, with a more accurate DNA model capable of capturing sub Kuhn length behavior. The scaling theory of activation energy is reevaluated especially in the weak electric field limit from the biased Rosenbluth sampling method. Both entropic and enthalpic terms of the free energy landscape show different scaling features in weak electric field regime, which are largely

neglected by previous studies. Chapter VII provides concluding remarks of the work described in this thesis with some suggestions on future research directions.

CHAPTER II

EXPERIMENTAL METHODS AND SIMULATION ALGORITHMS

2.1 Microchip Gel Electrophoresis

2.1.1 Microchip Device Assembly and Photo-initiated Gel Curing

Electrophoresis microchips (**Figure 4-b**) are fabricated following previously described methods (Lo & Ugaz, 2008). The microchips consist of three primary components: **a.** an etched glass microchannel (300 × 50 μm cross section) incorporating a separation channel with two side arms at one end for sample loading; **b.** a silicon substrate containing an embedded electrode array; and **c.** a PC board providing external connection to the on-chip electrodes (through wire bonding) via a 50-pin card edge connector and I/O block. The glass microchannel is bonded to the silicon substrate using UV-curable SK-9 Lens Bond (Summers Optical). An Omnicure Series1000 spot curing system with collimating lens attachment (EXFO) is used for gel casting inside the microchip. An Agilent 33220A function generator interfaced with a voltage amplifier (Trek Model 603) is used to generate waveforms for application of time varying electric fields. Wave functions with different periods are designed using the Agilent IntuiLink Waveform Editor and then upload and stored in the device. During the experiments, the waveforms are monitored using a Hewlett-Packard 54603B oscilloscope.

2.1.2 Experiment Automation, Fluorescence Detection and Image Analysis

Electrophoretic transport of the fluorescently labeled DNA is monitored using an Axioskop 2 microscope (Zeiss) with HBO 100 mercury arc lamp illumination, a fluorescein isothiocyanate (FITC) filter set, and a long working distance 10x objective. An ORCA-ER CCD camera (Hamamastu) is used for image acquisition. A motorized x-y translation stage is employed to enable synchronized positioning of the microchip and actuation of the camera shutter (Openlab; PerkinElmer).

For the sub 1kb DNA lengths employed here, we prepared desired concentration of crosslinked polyacrylamide gels by dilution from the 30 %T stock. The final gel reagent mixtures are certain volume of gel stock solution, 18.5 μL Solution B photoiniatior, 1.6 μL 10× TBE buffer, and DI water to make the total volume 30 μL. Before injecting this gel solution, the microchannel is first rinsed with Rain-X Anti-fog (SOPUS Products) followed by DI water. After injection, the polymerized gel interface is positioned by masking the glass surface above the injection ports with black tape. The microchip is then exposed to UV illumination for 1 min (intensity = 625 mW/cm^2), after which the black tape is removed and un-polymerized gel solution in the channel is replaced with 0.5× TBE buffer. The microchip is then exposed to UV again for another 11 min to complete polymerization of the gel inside the separation channel.

Samples are prepared by combining 3 μL of the DNA sample, 3 μL of YOYO-1 intercalating dye (Invitrogen) diluted to one tenth of the stock concentration (except in experiments involving titration of YOYO-1), 1.5 μL of β-mercaptoethanol, 1.5 μL 10× TBE buffer, and 5 μL of an appropriate dilution of the daunomycin stock solution. The

total volume is adjusted to 15 μL with DI water, and the mixtures are incubated for at least 30 min. Samples are then loaded into the microchip using a syringe and focused at the surface of internal electrode arrays by applying a low 1 – 1.2 V DC potential as described previously (Shaikh & Ugaz, 2006).

Individual snapshots acquired over the length of the separation channel during a single scan are joined together using Panavue software to produce a composite picture of the instantaneous in-gel band positions (**Figure 4-a**). A MATLAB code is then used to extract the intensity versus position profile along the centerline of the separation channel in the corresponding electropherograms (the centerline profile is used to avoid any sidewall band distortion). Each intensity peak is fitted to a Gaussian profile in order to obtain its center and variance for subsequent calculation of mobility and diffusion coefficients.

2.2 Atomic Force Microscopy

In order to attach DNA molecules on the surface of mica possessing the same negative charge, we first treated the fresh cleaved mica with 0.5 mg/mL poly-L-lysine solution (powder dissolved in DI water, Sigma-Aldrich, MW 30000-50000). After 30 min incubation time the mica surface was dried in a moderate flow of air. Then DNA complex sample was deposited on the polylysine-covered mica for 20 min, then washed with 30-50 μL DI water and dried in air. Sample is quickly imaged with in tapping mode (silicon tip, Multimode AFM with Nanoscope III controller, Bruker) with scan range

from 2 μm. DNA contour length was manually traced in ImageJ and measured with the Freehand Line module.

2.3 Brownian Dynamics Simulation of Overdamped Brownian Particles

Based on the Newton's second law, we could write a particle's equation of motion as,

$$ma(t) = m\frac{d^2r(t)}{dt^2} = F^D(t) + F^E(t) + F^B(t) \quad (1)$$

where m and $r(t)$ is the particle's mass and position vector, respectively. $F^D(t) = -\zeta v(t)$ is the drag force that linearly scales with the particle's velocity by the drag coefficient ζ. $F^B(t)$ is the random Brownian force representing the collisions from numerous surrounding particles. Followed fluctuation-dissipation theory, $< F^B(t) > = 0$ and $< F^B(t)F^B(t') > = 2k_BT\zeta/\delta t$ with δt denoting time step used in simulation (Kim, Panwar, Kumar, Ahn, & Lee, 2004). And the $F^E(t)$ is the force imposed by external field. For the over-damped assumption, the inertia term ($m\frac{d^2r(t)}{dt^2}$) becomes negligible and the equation of motion simplifies to:

$$\zeta\frac{dr}{dt} = F^E(t) + \sqrt{\frac{2k_BT\zeta}{\Delta t}}n \quad (2)$$

where n is a vector with zero mean and unit variance.

2.4 Prune-Enriched Rosenbluth Sampling and Monte-Carlo Simulation

A random configuration of DNA molecule is generated for the starting point of Monte Carlo simulation. We implemented Prune-Enriched Rosenbluth method (PERM) to generate a large number of DNA configurations. Compared with standard biased Rosenbluth sampling method (**Figure 5**), PERM introduced extra prune or enrich processes after adding new bead to the chain end (**Figure 6**) (Prellberg & Krawczyk, 2004).

Both methods require constant generation of trial configurations during the chain growing process follow the bending angle distribution. Different from the freely jointed chain model that allows any angle formed between neighbor segments, there is energy penalty in real chain to limit the bending angles to certain range. The bending energy(Y. Wang, Tree, & Dorfman, 2011) of the chain is defined as: $\frac{U}{k_B T} = \kappa \sum_{j=1}^{N-1} (1 - \cos\theta_j)$, where $0<\theta<180$ is the angle formed between segments. κ is the bending constant related to chain's Kuhn length l_K and bond segment length a as $l_K/a=2\kappa-1$. Based on this distribution we could express the distribution of bending angle (Frenkel & Smit, 2002; Tree, Muralidhar, Doyle, & Dorfman, 2013), $P(\theta)$ as:

$$P(\theta) = \frac{\kappa \exp\left[-\kappa\left(1-\cos\theta_j\right)\right]}{1-\exp(-2\kappa)} \tag{3}$$

In the chain growing steps, we calculate the introduced energy change for each generated configurations in order to update the Rosenbluth factor of the whole chain. The calculation of excluded volume energy involves determination the distance between

the new attempt segment and existing segments, which consumes large computation resources. Therefore we adopt a *verlet list* method (Tree, Muralidhar, et al., 2013), summarized in the following figure, to simplify the process. Generally (**Figure 7**) we first define a cutoff distance r_c, and a center bead. Any bead displaced in a distance to center bead close than r_c is grouped into the verlet list. So in the beginning of chain growth, the first bead is chosen as the center bead, as long as the new add bead is placed within a distance of r_c-w, the center bead is not changed and we only need to check overlapping between new bead and beads on the verlet list. Once any new bead exceeds the distance of r_c-w, it is chosen as the new center bead and the verlet list is cleared and recompiled for the new center bead.

CHAPTER III

DETERMINE ABNORMAL ENTROPIC DNA MIGRATION BEHAVIOR IN MICROCHIP GEL ELECTROPHORESIS*

It is pointed out in Chapter I that macromolecules exhibit different behavior when transporting in gel network with various structures. Most often people refer to two unique regimes regarding the relative size of the macromolecule gyration radius and the average gel pore. The first one is titled Ogston regime, where macromolecules migrate unperturbed in much larger pore network and the second regime is reptation regime where macromolecules reptate through relatively smaller pore. Decodes ago people began to discover an intermediate region lies between above mentioned regimes, where the average pore size of the sieving matrices comes closer to the macromolecules size. The underlying physics was explored with microfabricated device that mimic confining environment to reveal the entropical penalty as molecules squeeze into constrictions, which entitled this regime the name *entropic trapping* (ET). Although intrinsically interesting, these phenomena have not been widely explored in hydrogel matrices, a ubiquitous platform used in many analytical field, because it has not been clear how to link them to the underlying heterogeneous nanopore morphology. Here we introduce a theoretical model that establishes this connection, and describe microchip DNA electrophoresis experiments that demonstrate how ET effects can be exploited to yield a

---

* Parts of this chapter are reprinted with permission from Shi, N., & Ugaz, V. M. (2010) Tailoring the Nanoporous Architecture of Hydrogels to Exploit Entropic Trapping. *Physical Review Letters, 108,* 108101. Copyright 2010 American Physics Society.

surprising trend of increasing resolving power with DNA size (the opposite of what is conventionally observed).

3.1 Microchip Gel Electrophoresis as a New Platform to Study DNA Transport

Early gel electrophoresis studies helped identify qualitative features of DNA migration in the ET regime (Rousseau et al., 1997), but a detailed physical description has only emerged more recently with the introduction of so-called "nanofilter" devices (Ajdari & Prost, 1991; J. Han, 2000) where the hydrogel matrix was replaced by arrays of nanomachined fluidic channels whose height h periodically alternates between deep wells ($h \sim R_g$) and narrow slits ($h < R_g$) (**Figure 8-a**). In addition to enabling DNA migration to be directly probed in the ET regime, the greatly simplified geometry consisting of only two length scales (i.e., the heights of the deep and narrow regions) made it possible to develop improved physical models describing the observed phenomena. Despite the success of nanofilters, hydrogel matrices remain extremely attractive because they are easy to prepare and adapt for routine use, and because their nanoscale pore structure can be readily tailored by controlling polymerization conditions. But a comparable understanding of ET effects in hydrogels poses new challenges because their heterogeneous pore morphology is more challenging to capture than the idealized nanofilter geometry.

To address this, we begin by considering a theoretical framework developed to describe DNA transport through nanofilters in terms of a free-energy potential associated with travelling between adjacent pores, each of which is of a size $b \sim R_g$, by entering a confined interconnecting region where $b < R_g$ (i.e., the Kramers problem) (Craighead et

al., 1999; Fu, Yoo, & Han, 2006; Kasianowicz, Brandin, Branton, & Deamer, 1996; Panwar & Kumar, 2006; Sebastian & Paul, 2000; Stockmayer, 1976). Two key timescales emerge: (1) a time to migrate through the narrow space connecting the larger pores at each end (ν is the Flory exponent)

$$\tau_{mig} \sim M^{1+\nu} / E \tag{4}$$

(2) an activation time or "trapping lifetime"

$$\tau_{act} \sim \frac{1}{E^2} \exp\left(F_{act} / k_B T\right) \tag{5}$$

expressing the rate at which the energy barrier imposed by the narrow constriction can be overcome. E is the electric field strength, T is absolute temperature, k_B is Boltzmann's constant, end-activation is the dominant mode in the range of DNA and pore sizes of interest here (Panwar & Kumar, 2006). The free energy change is represented by $F_{act} = -T\Delta S - \Delta W$ containing an entropic contribution (ΔS) and a term associated with the electric potential (ΔW) (Fu et al., 2006). Our goal is to adapt this general framework to describe ET migration in a hydrogel network by establishing a link between the pore size distribution and the free energy change F_{act}.

We model the DNA migration path in the gel as a series of randomly dispersed loose regions and denser interconnecting zones (**Figure 8-b**), allowing the DNA migration path to be viewed as a *pseudo-nanofilter* incorporating a sequence of alternating large and small pores (the large pores are close to the DNA coil size, the small pores are smaller than the DNA coil size) but with the added ability to simultaneously vary the size of each (While the gel's nanoscale morphology embodies

details associated with the distribution of pore sizes present and their arrangement, the DNA migration path can be viewed as a continuous sampling of these pores comprising the network) . Expressing the entropic contribution to F_{act} in terms of a partition coefficient K' yields

$$\tau_{act} \sim \frac{1}{E^2}\exp\left(\frac{-T\Delta S - \Delta W}{k_B T}\right) = \frac{1}{E^2 K'}\exp\left(-\frac{\Delta W}{k_B T}\right) \tag{6}$$

where K' is related to both the DNA size and the gel pore size by (Liu et al., 1999)

$$\ln(K') \sim -M\left[\left(\frac{1}{r_i}\right)^{\frac{1}{\nu}} - \left(\frac{1}{r_j}\right)^{\frac{1}{\nu}}\right] \quad (r_i < r_j) \tag{7}$$

with r_i and r_j representing the small and large spaces, respectively (a pair of which comprise one pore unit; see **Figure 8-b**). The Flory exponent ν expressing how the DNA coil size scales with its length ($Rg \sim M^{\upsilon}$) (de Gennes, 1979) is determined using the Kratky-Porod model (Nkodo et al., 2001). Applying characteristic values for the persistence length (p = 50 nm) and contour length ($L_D = 0.34M$ [nm]) (Dorfman, 2010) of double-stranded DNA yields $R_g = 0.22M^{0.82}$.

3.2 Experimentals and Transport Modeling

3.2.1 Microchip Gel Electrophoresis

The basic microchip device assembly, experiment automation, fluorescence detection and image analysis are the same as described in previous chapter and different final hydrogel structures are prepared by combining various monomer concentrations and UV curing intensities.

3.2.2 Formation of the Transport Model

Followed the previous section, DNA transport in each pore unit $\mu_{i,j}$ is described by following equation:

$$\frac{\mu_{i,j}}{\mu_N} = \frac{\tau_{mig}}{\tau_{mig} + \tau_{act}} \tag{8}$$

An overall mobility is therefore defined as the average $\mu_{i,j}$ over the possible pore structures in gel defined by the probability density function:

$$\frac{\bar{\mu}}{\mu_N} = \frac{\langle \mu_{i,j} \rangle}{\mu_N} = \frac{\iint_{r_i<r_j} f(r_i) f(r_j) \frac{\mu_{i,j}}{\mu_N} \mathrm{d}r_i \, \mathrm{d}r_j}{\iint_{r_i<r_j} f(r_i) f(r_j) \mathrm{d}r_i \, \mathrm{d}r_j} = \frac{\iint_{r_i<r_j} f(r_i) f(r_j) \left(\frac{\frac{M^{1+\nu}}{E}}{\boxed{\frac{M^{1+\nu}}{E}} + \frac{C_1}{C_3} \frac{1}{E^2} \exp(-\Delta W / k_B T) \exp\left\{ C_2 M \left[\left(\frac{1}{r_i}\right)^{\frac{1}{\nu}} - \left(\frac{1}{r_j}\right)^{\frac{1}{\nu}} \right] \right\}} \right) \mathrm{d}r_i \, \mathrm{d}r_j}{\iint_{r_i<r_j} f(r_i) f(r_j) \mathrm{d}r_i \, \mathrm{d}r_j} \tag{9}$$

where C_1, C_2, and C_3 are constants associated with the scaling relationships for τ_{act}, K, and τ_{mig}, respectively, and the ratio C_1/C_3 can be replaced by a single constant C_4. The terms $f(r)$ represent the hydrogel's pore size distribution, which we assume is describable in terms of a Gaussian probability density function

$$f(r_i) = f(r_i) = \frac{1}{\sigma\sqrt{2\pi}} \exp\left(-\frac{(r-b)^2}{2\sigma^2} \right) \tag{10}$$

with r_i, $r_j > 0$. Characteristic values for the average pore size b and variance σ^2 are selected based on guidance from characterization studies we performed in comparable hydrogels (**Table 1**) (J. Wang, Gonzalez, & Ugaz, 2008). Neglecting the boxed term in the denominator of the upper integral yields an expression for the ratio of migration and

activation timescales τ_{mig}/τ_{act} (see **Eq. (8)**), the significance of which will be discussed shortly.

In evaluating the electric potential energy change (ΔW), we must consider the effect of hydrodynamic interactions that arise as a consequence of drag induced by the flow of surrounding ions within the tightly confined geometry of a narrow pore (van Dorp, Keyser, Dekker, Dekker, & Lemay, 2009), where we estimated the magnitude of these effects by referring to recent force measurements on DNA migrating through solid-state nanopores. The data reported in Fig. 4b of this paper suggest a relationship between the electrostatic force F_{elec} and pore radius R that follows $\frac{F_{elec}}{\Delta V}\left[\mathrm{pN}\cdot\mathrm{mV}^{-1}\right] \approx \frac{0.45}{\ln\left(R/a\right)}$, where a = 1.1 nm is the equivalent cylindrical radius of a DNA molecule. Since F_{elec} acts on the DNA over a length scale approximately on the order of the gel pore size, the change in electric potential energy associated with traveling a distance L^* through a pore can be estimated by $\Delta W = F_{elec}\, L^* \approx F_{elec}\,(2R)$, taking the potential change along the pore as $\Delta V = E\, L^*$. Since the magnitude of $\Delta W/k_BT$ is small, L^* is taken to be the average gel pore size, which is 15 nm based on our characterization studies in a 6 %T hydrogel (J. Wang et al., 2008) and $R = L^*/2$, yielding $\Delta W/k_BT \approx 1.9 \times 10^{-2}$.

We applied the following procedure to evaluate our transport model. First, we used **Eq. (8)** to fit experimentally obtained mobility versus DNA size data for fragments in the 100 – 1000 bp size range (**Figure 9**). The constant C_2 associated with the partition coefficient K can be evaluated for the case of specific pore morphologies (e.g., spherical, cylindrical, and slab; see Supporting Information), leaving only C_4 to be determined.

Notably, we find that these fits yield a reasonably constant value of $C_4 = 2.557 \times 10^5$ $[(\mathrm{bp}^{1+\nu})\cdot(\mathrm{V/cm})]$ across the entire ensemble of data only in the case where C_2 was evaluated assuming a cylindrical pore geometry ($C_2 = 0.85$ $[\mathrm{nm}^{1/\nu}\cdot\mathrm{bp}^{-1}]$). The fitting results agree remarkably well with our experimental data except at the smallest DNA size (100 bp) where migration is unlikely to be ET-dominated (**Figure 9**). Once C_2 and C_4 were determined, they were held constant during all remaining calculations so that the model (**Eq. (4)**) could be applied to predict the effects of varying the electric field and pore morphology, yielding the phase diagram plots shown in **Figure 10** and **Figure 11**.

3.3 Phase Diagram of DNA Transport Modes in Gel Electrophoresis

The transport model in **Eq. (8)** simultaneously captures the influence of ET, reptation, and Ogston sieving mechanisms because the migration and activation timescales are both represented. We do not impose a particular migration mechanism *a priori* but instead capture how the relative contributions from each mechanism are distributed. This is a critical point since the heterogeneous nature of a hydrogel's nanoporous morphology implies a coexistence of migration mechanisms, each of which is active in an appropriate pore size range governed by details associated with the gel composition and polymerization kinetics. These relative contributions become evident when the size dependence of mobility is expressed in terms of a ratio of the governing timescales associated with activation and migration (corresponding results showing the evolution of mobility with DNA size are shown in **Figure 11**). Recalling the physical

interpretation of the activation and migration timescales, we see that when $\tau_{mig} >> \tau_{act}$ DNA migration is dominated by the reptation-like process of traveling through the gel's narrow interconnecting regions. Conversely, if $\tau_{act} >> \tau_{mig}$ the migrating DNA is only weakly perturbed from its equilibrium coil configuration as more time is spent seeking to overcome the energy barrier associated with crossing from one large pore to another, resembling Ogston-like sieving behavior encountered when $R_g < b$. These effects can be globally represented in terms of a phase diagram depicting three distinct transport regimes based on τ_{mig} / τ_{act} value: ET, reptation, and pseudo-Ogston (**Figure 10-a**). Entropic trapping governs DNA migration in the intermediate regime where $\tau_{mig} / \tau_{act} \sim 1$. The calculated evolution of mobility with DNA size shows that migration is progressively driven away from the ET-dominated regime as E increases, accompanied by a decrease in the size dependence scaling (**Figure 10-b,** and **Figure 11-a**). This behavior is expected since the term representing τ_{act} is inversely proportional to E, ultimately yielding $\bar{\mu} = \mu_N$ in the high-field limit. The trends are also in agreement with experimental results reported by Slater, *et. al.* for gel electrophoresis of single-stranded DNA (Rousseau et al., 1997).

More importantly, our model also makes it possible to rationally identify hydrogels possessing morphological characteristics favorable for ET-dominated DNA transport. This is evident by comparing the ratio τ_{mig} / τ_{act} in hydrogels with identical composition cured at three different UV light intensities (5, 100, and 625 mW/cm^2). The calculated DNA mobility exhibits a size dependence more closely associated with ET in the hydrogel cured at a UV intensity of 625 mW/cm^2 than in the other gels, where

migration extends into the reptation-dominated regime (**Figure 10-c,** and **Figure 11**). These trends are not as straightforward as the electric field dependence because the nanoscale pore morphology is governed by the interplay between the pore size and its distribution (**Figure 10-b**), both of which in turn exhibit a complex dependence on polymerization conditions. Some insights into this interplay emerge by examining **Eq. (8)**. The term $[\left(\frac{1}{r_i}\right)^{1/\nu} - \left(\frac{1}{r_j}\right)^{1/\nu}]$ is small in gels with a narrow pore size distribution, resulting in a reduced activation timescale and diminished significance of ET effects ($\tau_{act} \rightarrow 0$ in the case of a monodisperse distribution, corresponding to pure reptation). Similarly, the individual terms $\left(\frac{1}{r_i}\right)^{1/\nu}$ and $\left(\frac{1}{r_j}\right)^{1/\nu}$ are small in gels with a large average pore size, again resulting in a decrease in the activation timescale associated with ET-dominated migration.

By revealing how the gel pore morphology influences the physical mechanism of DNA migration, the transport model in **Eq. (8)** provides a powerful tool to identify hydrogels where ET is dominant. We wanted to explore this capability by applying it to examine the extent to which ET effects can be harnessed to benefit a practical application such as gel electrophoresis. Separation efficiency can be expressed in terms of a resolution parameter $R = (x_2 - x_1) / (w_2 - w_1)$ describing the difference in distance traveled by two neighboring migrating species, x_i, relative to the sum of the half-widths of their associated peaks, w_i. Surprisingly, we find that R increases with DNA size in a hydrogel matrix whose pore morphology corresponds to ET-dominated migration (particularly at fragment sizes > 500 bp), while R either remains constant or decreases

with DNA size in matrices where reptation prevails (**Figure 12-a**). This ET-induced trend of increasing R with DNA size is the opposite of what is conventionally observed, and represents a highly desirable feature for separations (i.e., enhancing the ability to resolve large DNA fragments) that has not to our knowledge been previously reported.

To understand how this anomalous behavior is linked to the macromolecular transport mechanism, we express R in terms of mobility and diffusion parameters as follows (Luckey, Norris, & Smith, 1993)

$$R = \frac{1}{4}\left(\frac{\Delta\mu}{\mu}\right)\sqrt{\frac{LE}{2\left(\frac{D}{\mu}\right)}} \tag{11}$$

where $\Delta\mu$ is the mobility difference between two co-migrating species of interest (e.g., DNA fragments of different length), μ is their average mobility, and L is the distance traveled during separation (we use a value of 1 cm here to calculate resolution per unit length). Mobility and diffusion are conventionally related via the Einstein relationship, but this assumption is rarely valid because electrophoretic migration of DNA through a gel network does not strictly fall within the framework of Brownian equilibrium (Drougin, Slater, & Mayer, 1996). This is evident in our data where a log-log plot of D/μ versus M yields a linear scaling with slope –1 only at the smallest DNA fragment sizes, decreasing at a faster rate over the majority of the size range probed here (**Figure 12-b**). More importantly we find that D/μ decreases continuously over the entire DNA size range only when the hydrogel pore morphology is favorable for ET, while a plateau is reached at large fragment sizes in gels displaying reptation-dominated transport. Further differences in ET dominated migration are evident in the evolution of

$\Delta\mu/\mu$, which initially decreases, passes through a minimum in the vicinity of 500 bp, then increases again at the largest DNA sizes; whereas hydrogels that do not exhibit strong ET effects show a continuously decreasing trend (**Figure 12-c**). Taken together, these results suggest that the increase in R with DNA size observed during ET-dominated transport is linked to a highly favorable combination of decreasing D/μ (a quantity in the denominator of **Eq. (10)**) and increasing $\Delta\mu/\mu$ (a quantity in the numerator of **Eq. (5)**).

3.4 Summary

In this Chapter, we introduced microchip gel electrophoresis as an efficient approach to study DNA entropic trapping transport mode under confining environment. First, the heterogeneous structure of hydrogel allows us to further explore the structure effect on entropic trapping, whereas the length scale is too limited to achieve this in nanoslits arrays. Also, adapted the gel electrophoresis to a microchip platform enables us to simultaneously collect diffusion and mobility parameters of the transport process. We also proposed a transport model to describe the influences from different factors, such the hydrogel monomer-crosslinker concentration, UV intensity for gel casting and applied electric field strength. Based on the ratio of trapping time over migration time, we constructed a phase diagram of DNA transport mode in hydrogel and identify the windows where entropic trapping could happen. More importantly, this identification allows us to spot an anomalous resolution behavior in large DNA size range under entropic trapping mode. Results suggest that the increase in R with DNA size observed

during ET-dominated transport is linked to a highly favorable combination of decreasing D/μ (a quantity in the denominator of **Eq. (10)**) and increasing $\Delta\mu/\mu$ (a quantity in the numerator of **Eq. (10)**). Although resolution values are somewhat lower in gels influenced by ET, likely owing to the higher diffusivity generally associated with the erratic nature of this migration mode (Slater et al., 2000), the increasing trend with DNA size suggests potential to achieve improved separation performance (i.e., overcoming limitations on resolution and read length) through direct manipulation of the hydrogel's nanoscale pore architecture or by modulating the applied electric field over appropriate timescales associated with the activation and migration processes (Nixon & Slater, 1996; Slater et al., 2000). These insights may be useful to help guide the application of nanostructured materials (e.g., generated by self-assembly) to design matrices with pore morphologies specifically tailored to harness ET-dominated transport.

CHAPTER IV

SYNCHRONIZING DNA MIGRATION TO ACHIEVE IMPROVED SEPARATION AND MOLECULAR CONFORMATION PROBING*

4.1 Introduction

In Chapter III, we developed a transport model allowing us to define a DNA migration phase diagram connecting different modes with the sieving gel structures (pore size distribution) and applied electric field strength in gel electrophoresis. Our automated whole gel scanning method is able to collect image sequences for simultaneously calculation of mobility and diffusion coefficient. Within one specific regime where DNA molecular size is in the same range of the average pore size, i.e. entropic trapping regime, the separation resolution exhibits increasing trend in larger DNA size range. We also pointed out that despite this promising feature in separation, entropic trapping mode generates large diffusion along the separation due to the nature of random thermal motion to accommodate in restricted gel environment.

Entropy is fundamentally important in nearly all physical phenomena, but nature's exquisite control over the underlying randomness masks a complexity that has proven challenging to synthetically replicate. Almost half century ago, Kramer proposed a theory describing how a reaction system could overcome the reaction energy barrier by thermal or Brownian motion, which is then generalized to a problem of describing the

---

* Parts of this chapter are reprinted with permission from Shi, N., & Ugaz, V. M. (2010) An Entropic Force Microscope Enables Nano-Scale Conformational Probing of Biomolecules. *Small, 10,* 2553-2557.

escape rate from system metastable state in absence of external field. The existence of a characteristic system frequency reminds people of the possibility to coincide this with an external field oscillating in similar frequency, which is called stochastic resonance because of the random nature of the escaping events.

In this chapter we show how the stochastic dynamics associated with the inherent disorder from thermal motion, conventionally suppressed as an undesirable noisy background, can paradoxically be exploited as an enabling tool to manipulate macromolecular transport. This capability is the basis for a new probe of nanoscale molecular conformation based on stochastic resonance that makes it possible to finely resolve persistence and contour lengths, revealing new details about binding interactions between DNA and proteins at size scales much smaller than can be accessed by conventional methods.

4.2 Modeling DNA Entropic Migration in Gel Driven by Pulsed Electric Field

When the ET regime is accessed under a constant electric field, an inverted trend of increasing separation resolution with DNA size is observed (the opposite of what is conventionally seen), with a caveat that the absolute resolution values are below those obtainable in a gel matrix where transport is reptation-dominated in the low field limit (Shi & Ugaz, 2010) (**Figure 13-a** blue points; the resolution parameter R expresses the difference in distance traveled by two neighboring species relative to the sum of the half-widths of their associated peaks (Giddings, 1991)). But R increases significantly when the electric field is cyclically switched on and off at a period of $\Gamma = 5$ ms, reaching levels

that match or exceed those obtained in the reptation regime while simultaneously preserving the trend of increasing size dependence (**Figure 13-a**, red points; the time average electric field amplitude, E_{avg}, was held close to the value applied in our continuous field experiments). The enhancement coincides with a distinct mobility maximum at $\Gamma \sim 5$ ms that is most pronounced in the 500 to 1000 bp range, shifting toward lower Γ for smaller fragments (**Figure 13-b**). The modulation period associated with the mobility peak, displays a dependence on DNA fragment length (**Figure 13-c**). This effect is synergistically coupled with reduced diffusion relative the continuous field case (**Figure 13-d**).

Emergence of a size-dependent optimal modulation period Γ_{max} makes it possible to induce bi-directional transport of different sized DNA fragments. Conventionally, bi-directional transport has been achieved by designing non-symmetric systems, the operation of which usually involves applying backward and forward driving forces of different strengths (Thomas, Joswiak, Olson, Park, & Dorfman, 2013). In contrast, our approach involves modulating the timescales over which the electric field driving force is applied such that they are correlated with molecular-level transport phenomena (i.e., the activation time of hopping events). Specifically, the bi-directional transport presented here is achieved by periodically alternating between an electric field in the forward direction with Γ tuned to match resonance of the faster (leading) species, and a field in the reverse direction at a resonant period associated with the slower (trailing) analyte (**Figure 14-a**). The combined effect drives forward transport of a 300 bp DNA fragment (positive mobility) while a 600 bp fragment simultaneously travels backward

(negative mobility) (**Figure 14-b**). This bi-directional transport makes it possible to achieve a state in which separation resolution continually increases over time—an effect that can be precisely tuned to isolate DNA in a specific size range within a very short separation distance (**Figure 14-c**).

To show that these anomalous observations are manifestations of stochastic resonance, we must establish a connection between the optimal Γ and a characteristic system timescale associated with macromolecular transport. Our view of the nanoporous gel matrix architecture shown in **Figure 8** provides a starting point, enabling the fundamental framework developed to describe ET-dominated DNA transport in idealized nanoslit arrays to be applied by integrating over the pore size distribution (Fu et al., 2006; Shi & Ugaz, 2010). The free energy landscape $U(x)$ encountered by the DNA can therefore be expressed in terms of a series of double potential wells (Gammaitoni, Hanggi, Jung, & Marchesoni, 1998) whose depths represent the energy barrier at the entrance to the narrow interconnecting space between adjacent large pores (**Figure 15-a**). Assuming these transport events are uncorrelated (Gammaitoni et al., 1998; Olson, Ou, Tian, & Dorfman, 2011; Rousseau et al., 1997), an activation timescale is obtained from the instantaneous probability that a well is occupied for a time t, $\dot{P}(t) = -\gamma(t)P(t)$, where $P(t)$ is the probability of adopting a given energy state and $\gamma(t)$ is the escape rate (Zhou, Moss, & Jung, 1990). This quantity is more conventionally expressed in terms of a trapping time distribution.

$$\rho(t) = -\dot{P}(t) = \gamma(t)\exp\left(-\int_0^t \gamma(t')dt'\right) \tag{11}$$

Time-dependent escape rates $\gamma(t)$ corresponding to field-off and field-on conditions respectively are obtained from Kramers rate analysis (Fu et al., 2006; Kramers, 1940) as $\gamma_{off} \sim \exp(-\Delta U/k_B T)$, where $\Delta U = -T\Delta S$; and $\gamma_{on} \sim E^2 \exp(-\Delta U/k_B T)$, where $\Delta U = -T\Delta S - F_{elec}L^*$. Here, T is absolute temperature, k_B is Boltzmann's constant, E is the electric field strength (V cm^{-1}), ΔS and $F_{elec}L^*$ respectively represent the entropic and electric potential contributions to the free energy change associated with traveling a distance L^* through a pore ($\approx$ 1.9 x 10^{-2} $k_B T$ here (Shi & Ugaz, 2010)), and end-activation is dominant (Panwar & Kumar, 2006; Shi & Ugaz, 2010). In the interest of simplicity, our model does not explicitly consider thermally activated "backward" transport events (i.e., in the direction opposite to the driving force). These events occur with exponentially decaying probability (Zhou et al., 1990), and are indirectly accounted for in our fits to experimental data.

For simplicity, we consider a square wave (i.e., on-off) oscillatory electric field with amplitude $E(t)$ given as follows.

$$E(t) = \frac{E_0}{2}\left[1 - \mathrm{sgn}\left(\sin(\frac{2\pi}{\Gamma}t)\right)\right] \tag{12}$$

The initially symmetric double well energy landscape becomes distorted when a driving potential is applied, tilting along the electric field direction and experiencing a corresponding reduction in barrier height. Cyclically switching the electric field on and off therefore causes $\rho(t)$ to alternate between these states, introducing multiple peaks in the distribution curve spaced with a periodicity coinciding with the electric field actuation (**Figure 15-b&c**).

The DNA migration path through a surrounding gel matrix is viewed as a series of pore units (pairs of neighboring pores of radius r_i and r_j representing a large pore and narrow interconnecting space, respectively (Shi & Ugaz, 2010)) randomly dispersed in space, within which the pore sizes are distributed following Gaussian statistics with mean b and variance σ^2 (J. Wang et al., 2008).

Starting from **Eq. (7)**, the effect of applying a time varying electric field (i.e., cyclically switched on and off with period Γ) is incorporated by noting that $\tau_{mig}/\tau_{trap} \sim 1$ in the ET regime (Shi & Ugaz, 2010), implying that sequential activation and migration events rarely occur during the same field-on period. Instead, activated molecules remain trapped at the entrance to the narrow interconnecting region until the next field-on interval, yielding a residence time distribution characterized by peaks at odd multiples of the half period. Our assumption that the trap time distribution is peaked at odd multiples of $\Gamma/2$ enables $\rho(t)$ to be expressed in terms of the cumulative probability that activation will occur between the two possible trap time values.

$$\begin{aligned} \rho\{\tau_{trap} = \Gamma/2\} &= \int_0^{\Gamma/2} \rho(t)\,dt \\ \rho\{\tau_{trap} = (2n+1)\Gamma/2\} &= \int_{(2n-1)\Gamma/2}^{(2n+1)\Gamma/2} \rho(t)\,dt, \quad n = 1,2,3... \end{aligned} \tag{13}$$

This simplifies the analysis by allowing the ratio of migration and trap times in the mobility equation to be factored outside the integral over the trap time probability distribution.

$$\frac{\mu_{i,j}}{\mu_N} = \int \frac{\tau_{mig}}{\tau_{mig}+\tau_{trap}}\rho(t)dt = \frac{\tau_{mig}}{\tau_{mig}+\frac{\Gamma}{2}}\int_0^{\frac{\Gamma}{2}}\rho(t)dt + ... + \sum_{n=1}^{\infty}\frac{\tau_{mig}}{\tau_{mig}+(2n+1)\frac{\Gamma}{2}}\int_{(2n-1)\frac{\Gamma}{2}}^{(2n+1)\frac{\Gamma}{2}}\rho(t)dt \qquad (14)$$

Global transport throughout the entire gel can therefore be captured by integrating **Eq. (14)** over the distribution of all possible adjacent pore size combinations (i.e., pore size distribution), yielding the following expression for overall mobility $\langle\mu\rangle$

$$\frac{\langle\mu\rangle}{\mu_N} = \iint_{\substack{\text{pore size}\\ \text{distribution}}}\left(\frac{\tau_{mig}}{\tau_{mig}+\frac{\Gamma}{2}}\int_0^{\frac{\Gamma}{2}}\rho(t)dt + ... + \sum_{n=1}^{\infty}\frac{\tau_{mig}}{\tau_{mig}+(2n+1)\frac{\Gamma}{2}}\int_{(2n-1)\frac{\Gamma}{2}}^{(2n+1)\frac{\Gamma}{2}}\rho(t)dt\right)f(r_i)f(r_j)dr_i dr_j \qquad (15)$$

(We assume Gaussian pore size distribution with mean 9 nm, and variance 0.25 nm^2 based on our previous characterization studies (J. Wang et al., 2008)). The migration time is $\tau_{mig} = R_g/(\mu_N E) = C_1 M^{(1+\nu)}/E$, where R_g is the DNA's radius of gyration, and ν is a fitted exponent (a value of 0.82 is assumed (Shi & Ugaz, 2010)). The trapping times embedded within the expression for $\rho(t)$ are obtained from the reciprocal of the corresponding escape rates (i.e., $\gamma_{off} = (\tau_{trap,off})^{-1}$ and $\gamma_{on} = (\tau_{trap,on})^{-1}$), yielding

$$\tau_{trap} = \tau_{trap,off} + \tau_{trap,on} = C_2\exp(-T\Delta S/k_BT) + C_3\frac{1}{E^2}\exp\left(\frac{-T\Delta S - F_{elec}L^*}{k_BT}\right) \qquad (16)$$

The three remaining scaling constants are determined as follows:

$$\begin{aligned} C_1 &= 0.22\frac{3N_k}{\mu_0} = 0.22\frac{3L_D/l_k}{\mu_0} \approx 0.7425\times10^{-6} \\ C_2 &= x_m^2\frac{2\pi\zeta}{4\Delta W_s} \approx 0.5\times10^{-3} \\ C_3 &= D_0^{-1}\left(\frac{k_BT}{F_{elec}/E}\right)^2 \approx 0.69 \end{aligned} \qquad (17)$$

where $D_0 = k_B T/\zeta \approx 10^{-10}$ m^2 s^{-1} is the Zimm model diffusion coefficient, x_m is a scaling constant (chosen to be the average DNA radius of gyration (R_g = 30 nm for a 500 bp fragment length), and $\zeta = 6\pi\eta_s R_g$ is the DNA friction coefficient (η_s is the solvent viscosity) (Doi & Edwards, 1986). We also assume that $\Delta W_S \approx k_B T$, consistent with the physical scenario of an activated process. In subsequent calculations, the constants C_1, C_2, and C_3 were adjusted slightly to reflect a global best fit over the entire experimental data set, yielding C_1 = 1.5 x 10^{-6}, C_2 = 1 x 10^{-3}, and C_3 = 0.7.

Substituting these results into Equation (7) enables the mobility to be calculated as a function of DNA size. We numerically evaluated this expression over the first 300 periods of electric field modulation (beyond which $\int \rho(t)dt \to 1$), and found remarkably good agreement with mobility versus DNA length data obtained from microchip electrophoresis experiments performed over an ensemble of electric field actuation periods (**Figure 16**; some deviation is evident with 100 – 200 bp fragments whose size likely falls outside the ET regime). The MATLAB function *dblquad* was applied to execute the double integration between 0 and 50 nm pore size limits (values outside this range either are either not realistic or do not significantly change the results). The pore size averaged escape rate was obtained from $\gamma_{off} = \exp(\Delta W_S)/C_2$.

Our transport model can now be applied to understand the mobility peak observed at $\Gamma \sim 5$ ms (**Figure 13-b**). Analysis of the summation term in **Eq. (14)** reveals two contributions in each term: a time scale ratio (outside the braces), and a trap time probability (inside the braces). The emergence of a mobility peak becomes evident by separating the first term of the summation from the subsequent terms as follows.

$$\frac{\mu_{i,j}}{\mu_N} = \frac{\tau_{mig}}{\tau_{mig} + \Gamma/2}\left\{1 - \exp(-\frac{\Gamma}{2}\gamma_{off})\right\} + \frac{\tau_{mig}}{\tau_{mig} + 3\Gamma/2}\left\{\exp(-\frac{\Gamma}{2}\gamma_{off}) - \exp\left[-\frac{\Gamma}{2}\gamma_{off} - \frac{\Gamma}{2}(\gamma_{off} + \gamma_{on})\right]\right\} + \ldots\ldots \quad (18)$$

Increasing Γ in the first term (representing the probability of an activation event (Tessier & Slater, 2002)) simultaneously decreases the time scale ratio and increases the trap time probability, consistent with emergence of a maximum value (the value of this term is maximized when $\gamma_{off}\ \Gamma_{\max}/2 = 1.145 \sim 1$; obtained by seting first derative over ($\gamma_{off}\ \Gamma_{\max}/2$) for this term to zero and noting that $\gamma_{\text{off}}\ \tau_{mig} = \tau_{mig}/\tau_{trap,off} \sim 1$ in the ET regime). In contrast, the magnitude of both contributions becomes smaller in all subsequent terms as Γ increases, acting to smooth out the local maximum generated by the first term. The mobility peak therefore corresponds to intermediate γ_{off}, and its prominenence at DNA lengths 500 bp and above is explained by the size-dependent escape rate (γ_{off} increases as the molecules become shorter).

In addition to displaying good agreement with experimentally measured mobilities, evaluating our transport model as a function pore size distribution breadth reveals critical fundamental insights (**Figure 17-a**). First, in each case the mobility peak is positioned such that $\gamma_{off}\ \Gamma/2 \sim 1$, shifting to larger Γ as the distribution becomes more polydisperse. This clear link between the electric field actuation period and the characteristic trap time (the system timescale), combined with their importance in dictating placement of the mobility peak, compellingly confirms the governing role of stochastic resonance (further echoed by the simulations of Tessier and Slater (Tessier & Slater, 2002)). The DNA size dependence of the actuation period associated with the mobility peak, $\Gamma_{\max}$, is also captured (**Figure 17-b**).

Our model shows how the gel pore morphology shapes the global energy landscape, and hence macromolecular transport (**Figure 17-c**). As the pore size becomes increasingly polydisperse, the corresponding entropic energy barrier distribution broadens accompanied by an increase in the average well depth (trap strength) ΔW_S due to the growing population of small sized pores (very large and very small pores are excluded since the experimentally measured pore sizes are well-fit by a Gaussian distribution(Shi & Ugaz, 2010; J. Wang et al., 2008)). The cumulative residence time probability $\Phi(t) = \int_0^t \rho(t')dt'$ increases most slowly at small Γ (where multiple actuation cycles are needed to cross the energy barrier) and in gels with broader pore size distributions (reflecting higher average ΔW_S) (**Figure 17-c**, insets). The distribution of entropic energy barriers was generated by sampling a Gaussian ensemble of 10^4 pore units (i.e., r_i and r_j combinations), after which ΔW_S was calculated for each as follows with $C_4 = 0.85$ (Duke, Austin, Cox, & Chan, 1996; Shi & Ugaz, 2010).

$$\Delta W_S = MC_4 k_B T \left[\left(\frac{1}{r_i} \right)^{\frac{1}{\upsilon}} - \left(\frac{1}{r_j} \right)^{\frac{1}{\upsilon}} \right] \tag{19}$$

4.3 The Idea of Entropic Force Microscope

In previous section, we have observed that in entropic trapping mode, electrophoretic mobility exhibit peak value at certain period associated with external oscillating field. This characteristic period, named Γ_{max}, is related to molecular size and the pore structure. As shown in **Figure 17**, there is a linear fitting between the molecular

size and the Γ_{max}, which inspires us to explore the possibility of using this phenomena to probe the molecular conformational change in a much easier way to match the entropic hopping events with a pulse electric field and read the maximum mobility peak as the indication of molecular size, i.e. entropic force microscope (**Figure 18**).

We demonstrate our approach by applying it to examine interactions between double-stranded DNA and two distinct binding agents: the intercalating chemotherapy compound daunomycin (Eckel et al., 2003; Sischka et al., 2005), and the fluorescent bis-intercalator dye YOYO-1 (Günther, Mertig, & Seidel, 2010). The experimental protocol is operationally simple, involving recording transport of the bound complex through a nanoporous hydrogel matrix under a time-varying electric field (first held constant, then switched on and off over a sweep of periods Γ) and determining the corresponding mobility μ (an automated microchip-based platform enables a complete set of data to be acquired in 10 – 20 min; Methods). **Figure 19-a** shows how the mobility of a 600 base pair DNA fragment becomes significantly altered upon binding with daunomycin (electric field conditions and surrounding nanopore morphology are chosen to yield ET-dominated transport (Shi & Ugaz, 2010)). Namely, a distinct mobility peak appears at a specific electric field actuation period $\Gamma_{\max}$ that shifts to lower values of Γ as the daunomycin loading is increased. A different trend is observed upon binding with YOYO-1, with $\Gamma_{\max}$ approaching higher values only at very high loadings (**Figure 19-b**).

These mobility peaks emerge as a consequence of size-dependent SR triggered at a specific electric field actuation period satisfying the resonant condition $\gamma_{off}\,\Gamma_{\max}/2 \sim 1$.

Quantitative structural information is therefore embedded in the value of Γ_{max}, and these details are obtainable by establishing the relationship between Γ_{max} and molecular size (expressed in terms of the radius of gyration R_g) using mobility measurements acquired from native DNA fragments of known length (**Figure 19-c**). The bound complex's R_g can then be linked to its characteristic Γ_{max} value, and subsequently mapped to the corresponding persistence length p and contour length L via the Kratky-Porod worm-like chain model (**Figure 20)**

$$R_g = \frac{1}{2}\sqrt{2pL\left[1 - \frac{p}{L}\left(1 - \exp(-L/p)\right)\right]} \tag{20}$$

Mobility measurements acquired under a constant electric field independently connect μ and the number of Kuhn segments N_k via $\mu = \mu_0 / 3N_k$ (μ_0 is the free solution mobility ~ 3.3×10^{-4} cm^2 V^{-1} s^{-1}]) (Rhee & Ware, 1983; Viovy, 2000). Native DNA fragments of known length are again probed to determine $N_k = L / l_k$ (l_k is the Kuhn segment length; L [nm] = 0.34 times the DNA length in base pairs, $l_k = 2p$ = 100 nm for the native dsDNA) (Shi & Ugaz, 2010), enabling the bound complex's N_k to be inferred from its constant field mobility (**Figure 19-c, inset**). These two relationships, obtained under time-varying and constant electric field conditions in the ET regime respectively, are then simultaneously evaluated to determine p and L.

Structural parameters obtained in this way reveal important insights about how each compound interacts with DNA via distinct binding mechanisms (**Figure 21-a** and **Table 2**). First, daunomycin shortens the contour length while increasing backbone rigidity (higher persistence length), likely reflecting alterations to the DNA structure that

emerge as a consequence of adduct formation mediated by the anti-photobleaching additive β-mercaptoethanol (BME). Owing to its function as a strong reducing agent, the aldehyde group generated from oxidation of BME can become available to induce covalent bonding between daunomycin and one of the dsDNA strands while hydrogen bonding is maintained with the other strand (Cullinane, Cutts, Panousis, & Phillips, 2000; Minotti, Menna, Salvatorelli, Cairo, & Gianni, 2004; Zeman, Phillips, & Crothers, 1998). Formation of an adduct complex via a cross-linking mechanism other than hydrogen bonding (intercalation) yields a more compact DNA structure—a significant discovery that suggests our method is capable of finely resolving structural alterations associated with adduct formation in DNA fragments too small to readily probe via conventional methods. In contrast, YOYO-1 increases DNA chain flexibility (smaller persistence length) while slightly increasing its contour length, consistent with a bis-intercalation mechanism. A key conclusion from these measurements is that YOYO-1 does not appear to dramatically alter the DNA conformation at low to moderate loadings employed in conventional fluorescent labeling (loadings at least 3x lower than tested here are typically used, Methods). Since the DNA sizes we employ are too small to analyze using single-molecule force measurements, we validated our entropically determined structural parameters by comparing them with data obtained from AFM images (**Figure 21-b**). Contour lengths determined using the two methods agree remarkably well (**Table 1**; AFM is unable to unambiguously quantify persistence lengths), especially considering the operational simplicity of our approach.

4.4 Summary

In this Chapter, we use our transport model to identify entropic trapping migration behavior in microchip gel electrophoresis. Besides noticing promising resolution trend in large size DNA range, we state that the overall resolution is diminished by the high diffusion coefficient. This high diffusion originates from the random thermal motion the macromolecules undertake to overcome local energy barrier and hop between constriction regions in gel. From common sense, this system noise needs to be quenched for improved performance. Counter-intuitively, we introduced the idea of stochastic resonance in the entropic trapping mode to globally synchronize the noisy hopping event with external oscillating electric field. Apart from doubling the predicted resolution performance, we further observe the existence of a mobility peak associated with certain period value of the applied pulsed electric field. Based on the transport model adapted to the pulsed filed activation, we show that the external driving force and the internal system activation time scale obey the resonance condition. This capability lays a foundation for a sensitive probe of nanoscale molecular conformation, revealing previously unseen details about DNA-protein binding interactions at size scales far below the limits of conventional techniques. A key breakthrough is that our method is the first practical application of this stochastic resonance in entropic trapping transport of micromolecules (previously studied, but only theoretically), yielding a new tool to “image” nanoscale details of biomolecular conformation.

CHAPTER V

BROWNIAN DYNAMICS SIMULATION OF PARTICLES TRANSPORT IN CHANNELS WITH ALTERNATING CONFINEMENTS*

5.1 Introduction

Entropically mediated phenomena are of emerging interest as a driving force for micro- and nano-scale transport, but their underlying stochastic nature makes them challenging to rationally manipulate and control. In Chapter IV, we show that stochastic resonance offers an intriguing avenue to overcome these difficulties by establishing a clear connection between the system response (the output) and an externally imposed driving force (the input). During developing model for molecule transport with stochastic resonance, we found that previous studies have generally adopted a signal-processing viewpoint to classify the output in terms of a signal-to-noise ratio, but this link does not convey information that is immediately useful to infer parameters relevant to transport. In this chapter, we address this issue by applying Brownian dynamics simulations to elucidate the residence time distribution encountered by a particle as it travels through a channel incorporating periodic constrictions. A sinusoidal longitudinal driving force is applied with a superimposed continuous orthogonal component, making it possible to identify frequency and amplitude conditions where temporal coherence with the particle's motion can be achieved. This resonant state reflects a synergistic

---

* Parts of this chapter are reprinted with permission from Shi, N., & Ugaz, V. M. (2010) Entropic Stochastic Resonance Enables Trapping Under Periodic Confinements: Brownian-dynamics Study. *Phys. Rev. E, 89,* 012138. Copyright 2010 American Physics Society.

combination of geometry and driving force that can be exploited to confine species at discreet locations, offering new possibilities for directed manipulation.

Transport of particles and particle-like species in micro- and nano-scale confined environments occurs in a variety of contexts including translocation of small biomolecules through nanopores (Harms et al., 2011), biological ion channels (Lee, Choi, Han, & Strano, 2010), and DNA separations in nanofilters (Fu et al., 2006). These systems impose an energy barrier associated with reduced conformational freedom in a constriction connecting two neighboring larger spaces. Transport under these conditions is characterized by discreet "hops" across the constricted regions—a process often referred to as entropic trapping. A weak external driving force can alter this free energy landscape, partially compensating for the entropic penalty. Kramers (Kramers, 1940) considered this mode of transport and obtained an expression for the characteristic hopping frequency (escape rate) in terms of the entropic energy barrier, the driving force, and the species' thermal energy. But the escape rate distribution is inherently broad, reflecting the underlying random thermal motion that enables successful hops to occur.

More recent work has suggested the intriguing possibility that randomness can play a constructive role, enabling the system response to be rationally manipulated by applying a periodic external driving force in a controlled manner (Gammaitoni et al., 1998). In this way, it is possible to achieve synchronization between the hopping events and the driving force, a condition known as stochastic resonance (SR). In his pioneering work (Burada, Schmid, Reguera, Rubi, & Hänggi, 2009; Burada et al., 2008; Reguera et

al., 2006), Hänggi, et. al. demonstrated that SR could be achieved in entropy-dominated particle transport actuated by a periodic driving force with a superimposed continuous orthogonal component, yielding enhanced spectral amplification. Unfortunately, the signal-processing viewpoint traditionally used to describe these resonant effects (e.g., in terms of maximizing the signal-to-noise ratio) does not convey information immediately useful to connect resonance with transport parameters relevant to particle manipulation. From the experimental side, people demonstrated emergence of stochastic resonance behavior in a bistable electronic device, i.e., the tunnel diode and also the dynamics of short polymer translocation driven by oscillating force (Lanzara, 1997; Pizzolato, Fiasconaro, Adorno, & Spagnolo, 2013; Spagnolo & Mantegna, 1995). These studies revealed many intriguing phenomena such as resonant crossing of the energy barrier and enhanced diffusion by manipulation of the system noise strength (Dubkov & Spagnolo, 2005; Fiasconaro & Spagnolo, 2011; Hasegawa & Arita, 2012). However, because most of these studies are focused on the noise strength effect, their results are not straightforwardly translatable to many practical settings (e.g., biological operations) where there is little or no flexibility to modulate the system temperature. Here we address above raised issues by focusing on the residence time distribution of Brownian species in a spatially periodic array of constrictions under the influence of a temporally periodic longitudinal driving force with a constant transverse component (Burada et al., 2009; Burada et al., 2008; Reguera et al., 2006), and employing Brownian dynamics simulations to elucidate how proper selection of parameters associated with both domains of periodicity make it possible to induce resonance associated with the escape

rate from the local energy barrier. A key difference between our approach and those in aforementioned references is that the temperature (noise strength) in our system remains constant. We therefore achieve SR by tuning the frequency and amplitude of an external periodic force, in contrast to previous studies where SR effects are accessed by tuning the noise strength. Our formulation makes it possible to design systems of particular relevance to biological and separation applications where the underlying randomness associated with entropic phenomena can be exploited to direct species transport in a controlled way.

5.2 Stochastic Resonance in Single Constriction Geometry

We begin by considering a 2D topology consisting of upper and lower bounding surfaces that impose periodically spaced constrictions (**Figure 22-a**). The resulting cross-sectional profile is defined as follows (Burada et al., 2008)

$$w_{\pm} = \mp L_y \left(\frac{x}{L_x}\right)^4 \pm 2L_y \left(\frac{x}{L_x}\right)^2 \pm \frac{b}{2} L_x \tag{21}$$

where the upper and lower walls of the channel are denoted as w_+ and w_-, respectively. The constriction width at $x = 0$ is defined by the product $L_x\ b$, where L_x is the axial distance from the constriction to the maximum channel width position ($x = L_x$ or $-L_x$). The product $2\ L_y$ expresses the reduction in channel width from $x = L_x$ or $-L_x$ to the constriction at $x = 0$.

Transport is formulated in terms of the Langevin equation describing over-damped particle motion

$$\gamma \frac{d\mathbf{r}}{dt} = -G\mathbf{e}_y - F(t)\mathbf{e}_x + \mathbf{F}_B \tag{22}$$

$\mathbf{F_B}$ is the Brownian force with zero mean and correlation function $< F_B(t)F_B(t') > = 2k_BT\gamma\delta(t-t')$, k_B is Boltzmann's constant, T is absolute temperature, γ is the friction coefficient, and $\boldsymbol{r}$ represents the position of the particle (Cartesian coordinates with unit vectors $\mathbf{e_x}$ and $\mathbf{e_y}$ in the x- and y-directions respectively), G is the magnitude of the transverse force, and the longitudinal sinusoidal force has the form $F(t) = F_0 \sin(\Omega t)$. The last term on the right hand side of **Eq. (22)** expresses the zero-mean Brownian force.

Eq. (21) & Eq. (22) are made dimensionless using a base length scale L_x, time scale $\gamma L_x^2 / k_B T$, and force $k_B T / L_x$, yielding

$$\tilde{w}_{\pm} = \mp\varepsilon\tilde{x}^4 \pm 2\varepsilon\tilde{x}^2 \pm \frac{b}{2} \tag{23}$$

$$\frac{d\tilde{\mathbf{r}}}{d\tilde{t}} = -Pe_y\mathbf{e}_y - Pe_x(\tilde{t})\mathbf{e}_x + \tilde{\mathbf{F}}_B \tag{24}$$

in terms of the dimensionless variables $\tilde{w}$, $\tilde{x}$, $\tilde{r}$, $\tilde{t}$, where $\varepsilon = L_y / L_x$. Two Péclet coefficients are defined as $Pe_y = G\ L_x\ /\ k_BT$ and $Pe_x(\tilde{t}) = \tilde{F}_0\sin(\tilde{\Omega}\tilde{t})$, with $\tilde{F}_0 = F_0 L_x / k_B T$. Note that γ and F_0 are both species dependent. Following Kim, et. al. (Kim et al., 2004), we express the Brownian force as $F_B = \left(\frac{4\gamma k_B T}{\Delta t}\right)^{1/2} \boldsymbol{n_i}$, where Δt is the time step used in the simulation and $\boldsymbol{n_i}$ is a random vector with each component uniformly distributed over [–1, 1]. We then obtain a scaled Brownian force $\tilde{F}_B = \left(\frac{4}{\Delta\tilde{t}}\right)^{1/2} \boldsymbol{n_i}$.

Next we express the energy landscape by assuming a pseudo-homogeneous field (i.e., forces do not vary in the *y*-direction). In this way, the *y*-averaged potential can be used to obtain a simplified expression in the absence of a longitudinal force that depends only on the particle's *x* position (Burada et al., 2009).

$$U(x) = -(k_B T)\ln\left(\frac{\int_{w_-}^{w_+} e^{-U(x,y)/k_B T}\, dy}{w_- - w_+}\right) \tag{25}$$

Substituting $U(x,y) = Gy$ into above equation and scaling the energy by $k_B T$ enables the landscape to be expressed by the 1D relationship

$$\tilde{U}(\tilde{x}) = -\ln\left[\frac{1}{(\tilde{w}_+ - \tilde{w}_-)Pe_y}\left(e^{-Pe_y\tilde{w}_-} - e^{-Pe_y\tilde{w}_+}\right)\right] \tag{26}$$

where the maximum and minimum energies are located at $\tilde{x}$= 0 and ± 1, respectively (**Figure 22-b**). The trap strength is therefore controlled by the magnitude of *G* in the unperturbed system.

Now we consider application of a time-periodic longitudinal driving force and ask how its period $\tilde{\Gamma} = 2\pi/\tilde{\Omega}$ can be tuned to match the escape rate from the local energy barrier (i.e., $\frac{2\pi}{\tilde{\Omega}} \sim 1/\tilde{r}_K$, where $\tilde{r}_K$ is the escape rate) (Gammaitoni et al., 1998) .In the absence of the longitudinal force, the scaled escape rate in the energy landscape described by **Eq. (25)** is given by Kramers' formula.

$$\tilde{r}_K = \frac{\sqrt{-\left(\left.\frac{d^2\tilde{U}(\tilde{x})}{d\tilde{x}^2}\right|_{\tilde{x}=0}\right)\left(\left.\frac{d^2\tilde{U}(\tilde{x})}{d\tilde{x}^2}\right|_{\tilde{x}=1}\right)}}{2\pi}\exp\left(\left.\tilde{U}(\tilde{x})\right|_{\tilde{x}=1} - \left.\tilde{U}(\tilde{x})\right|_{\tilde{x}=0}\right) \tag{27}$$

A trial-and-error approach is sufficient to identify a resonance condition associated with parameter values Pe_y = 0.1, $\tilde{\Omega}$= 0.01, and $\tilde{F}$=0.05. Since the system state at SR is sensitively impacted by these values (**Figure 23-a**), this method is appropriate for the purposes of our study where the primary goal is to illustrate the key phenomena. Substituting Pe_y = 0.1 into **Eq. (27)** yields a characteristic escape rate of $\tilde{r}_K \sim 10^{-4}$ in the unperturbed system. This analysis suggests that an order of magnitude increase in the escape rate is attainable by lowering the energy barrier via the periodically applied driving force $\tilde{r}_K = \left(2\pi/\tilde{\Omega}\right)^{-1} = 1.6\times10^{-3}$. Notice that we ensure the model is applied only in the entropic regime by imposing a relatively small transverse force Pe_y (Burada et al., 2009).

5.3 Stochastic Resonance-mediated Trapping

A key manifestation of SR is attainment of coherence between a species' oscillatory motion and an imposed periodic driving force, suggesting potential to achieve selective immobilization or separation in an appropriately designed microchannel network. To explore this possibility in the context of the simplified geometry depicted in **Figure 22-a**, we employed Brownian dynamics simulations to monitor particle displacements over a simulation time encompassing 250 driving force periods (**Figure 23-a**). These data were analyzed to identify times associated with transit through

the energy maxima and minima positions in **Figure 22-b** ($\tilde{t}_{x=0}$ and $\tilde{t}_{x=\pm1}$, respectively). A histogram of the time intervals between each passage through successive energy maxima and minima ($\Delta\tilde{t}_0$and $\Delta\tilde{t}_{\pm1}$, respectively) reveals a narrow distribution centered around a mean value close to the driving force period, $\tilde{\Gamma} = 628$ (**Figure 23-b**). This high degree of synchronization is accompanied by a phase shift between the applied driving force and particle displacement through the microchannel. Closer examination of our data reveals a characteristic phase lag of $\tilde{t}_{lag} \approx 100$ (**Figure 23-c**), in good agreement with the theoretically predicted value obtained from $\tilde{t}_{lag}\times\widetilde{\Omega} = \bar{\varphi} \approx \arctan(\widetilde{\Omega}/2\tilde{r}_K)$ (Gammaitoni, Marchesoni, Martinelli, Pardi, & Santucci, 1991).

5.4 Trapping in a Geometry with Repeating Constriction Units

We next considered a topology containing repeated constriction units bridging adjacent segments of wider cross-section (**Figure 24-a**). Transport between successive constriction units can be achieved by applying a driving force with different phase values in each unit as follows

$$\tilde{F}_i(\tilde{t}) = \tilde{F}_0 \sin\left(\tilde{\Omega}\left(\tilde{t} - \tau_i\right)\right) \tag{28}$$

where τ_i (i = 2, 3, 4) compensates for the time associated with each particle's entry into each unit (τ_1 = 0 by default since particles are initially located in unit 1). The average value of τ is determined from the aforementioned synchronization between transport and the applied driving force.

We determined the τ_i values by simulating the displacements of an ensemble of 400 particles through the microchannel geometry shown in **Figure 24-a** and recording the time of initial entry into each subsequent constriction unit. Once a particle in constriction unit *i* travels beyond the energy minimum in the adjacent zone of larger cross-section, the driving force is switched to a value corresponding unit $i + 1$ with τ_{i+1} (**Eq. (28)**), while the transverse force is held constant. The resulting distributions (**Figure 24-b**) confirm that transit times are narrowly distributed with average values $<\tau_3>$ = 300 and $<\tau_4>$ = 500, consistent with the results in **Figure 23-c**. As a result of resonance behavior, the time interval during which species travel between $\tilde{x}_{max}$ and $\tilde{x}_{\pm min}$ in each constriction unit (e.g., $\tilde{x} = 0$ and $\tilde{x} = \pm 1$ in **Figure 22-b**) is narrowly distributed. In this framework, τ_2 represents the time to travel from $\tilde{x}_{max}$ to $\tilde{x}_{+min}$ within the first unit (i.e., corresponding to $< \tilde{t}_0 - \tilde{t}_{\pm 1} > \sim 100$ in **Figure 24-b**), whereas the subsequent τ_i correspond to the transit times associated with traveling between $\tilde{x}_{\pm min}$ in successive units (i.e., $< \tilde{t}_{+1} - \tilde{t}_{-1} > \sim 200$ in **Figure 24-b**). By applying these τ_i values, species can be successfully trapped at prescribed locations (**Figure 25**).

An important potential application of these resonance phenomena is separation of a target species from different-sized background components. To explore feasibility of employing SR in this way, we characterized trapping stability and sensitivity to the applied driving force by simulating an ensemble of 400 particles during 100 driving force periods over a range of peak amplitude values ($\tilde{F}_0$) in the geometry shown in **Figure 24-a**. The influence of $\tilde{F}_0$ on trap stability in the 4th constriction unit is visually depicted by the trajectories in **Figure 26-a**. Stable trapping is only sustained at

resonance (Pe_y = 0.1, $\widetilde{\Omega} = 0.01$, $\tilde{F}_0 = 0.05$), while particles escape the trap and diffuse away with non-trivial probability under other conditions. These trends are clearly seen when displacements are quantified in terms of a survival percentage (i.e., the instantaneous fraction of species that remain trapped, **Figure 26-b**). The onset of trapping is signaled by an initial jump in survival percentage from zero to unity as $\tilde{F}_0$ approaches the resonant value of 0.05, but the weak confinement gives way to a steady decrease in survival percentage toward zero at a rate dependent on the extent to which $\tilde{F}_0$ deviates from resonance. In contrast, trapping stability dramatically increases once resonance is established, with the survival percentage remaining solidly near unity for over 100 driving force periods. Trapping is extremely selective owing to sensitive dependence of the resonant state on system parameters (e.g., a 10% decrease in $\tilde{F}_0$ from 0.05 to 0.045 enables escape from the trap after ~ 10 driving force periods).

5.5 Summary

In this chapter, we have explored resonant transport in a microchannel geometry incorporating a spatially periodic array of constrictions under the influence of a temporally periodic driving force. Proper selection of the parameters associated with both domains of periodicity makes it possible to induce stochastic resonance associated with escape from the local energy barrier. Instead of the concept of signal to noise ratio employed in most previous literature involving SR, we have examined the rate of species displacement through the energy landscape and its degree of synchronization with the periodically applied driving force. The period of particle motions and its phase

differences with the driving force are quantified by Brownian dynamics simulations, yielding results that display good agreement with the established theoretical understanding of SR. We demonstrated application of this idea in the context of a microchannel geometry incorporating periodic constrictions and modulated the periodic driving force at a different phase in each constriction unit so that particles become selectively confined at prescribed locations within the network.

To obtain a sense of scale for these effects we consider transport of a 50 nm species carrying a charge of 10e in the constriction unit geometry of Figure 1a, where the microchannel is 3 μm wide at $\tilde{x} = \pm 1$ and 0.5 μm wide at $\tilde{x} = 0$, and where L_x = 5 μm. A potential on the order of 1 mV would required to actuate transport between successive energy minima in this configuration, suggesting that a standard AA-size battery could be capable of providing a sufficient driving force to direct transport through an array of 1,000 constriction units (~ cm scale). SR-based approaches also may also help overcome limitations of electrostatic-based trapping because low-salt buffering conditions are not required to augment the electrostatic double layer. This level of robustness, combined with the ability to achieve highly stable and selective trapping, suggests the intriguing possibility of exploiting SR effects as a new approach to perform manipulation and sorting at the microscale.

CHAPTER VI

MONTE CARLO SIMULATION OF ENTROPIC DNA TRANSPORT IN NANOFILTERS

6.1 Introduction

As shown in both Chapters I and III, microfabricated nanoslit arrays provide a novel way to separate macromolecules, and more importantly we can investigate the physics underlying the abnormal entropic transport mode utilizing its geometric structure that is close to macromolecule size. Besides experiments, computer simulations have been applied to further study the dynamics as the molecules squeeze into the shallow regions in the arrays. Results of these studies reveal the free energy landscape of this process and suggested that the activation energy to escape the entopic trap scales inversely with the applied electric field. However, these studies (both experiments and simulations) are conducted at relatively high electric fields and for simulation the models employed do not fully capture sub-Kuhn length effects as molecules migrate though the shallow part in the channel. Therefore in this chapter we propose a Monte Carlo simulation of long molecule transport in 3D nanoslit arrays driven by a wide range of electric field strengths. We modeled the molecule as series beads connected by inextensible rod with length much less than the molecular Kuhn length in order to incorporate sub-Kuhn length dynamics. These simulation results reveal a new scaling behavior between activation energy and the applied electric field from the analysis of confinement and electrostatic energy.

6.2 Simulation Algorithm

6.2.1 Geometry of the Nanofilter and Eelectric Field Distribution

The 3D structure is depicted in **Figure 27**. The channel is composed of alternating deep and shallow regions sharing the same length in the *x*-direction. The depth of the shallow region is set to 100 nm, comparable to the Kuhn length of dsDNA, and the depth of deep part is set to 2000 nm, large enough for lambda DNA with R_g close to 700 nm (Dorfman, 2010). The width of the channel is 2000 nm through the length so that DNA molecule will not experience any constriction in the *y*-direction. In order to determine the electric field distribution inside this channel, we applied a periodic boundary condition where the section in the red box is selected to add a fixed potential. The Laplace equation of potential $\frac{\partial^2 \Psi}{\partial x^2} + \frac{\partial^2 \Psi}{\partial y^2} + \frac{\partial^2 \Psi}{\partial z^2} = 0$ is solved in COMSOL using a predefined extra fine triangle mesh. The inlet boundary (left) is grounded and the outlet boundary (right) supplies an imposed potential V so that $\frac{V}{L0} = E_{ave}$. Zero flux boundary conditions are applied elsewhere at the channel walls. The result of electric field was interpolated to a series of regular grid points with 20 nm intervals in *x*, *y* and *z* directions.

6.2.2 DNA Model and Parameters

DNA is modeled as N beads connected with $N - 1$ inextensible rods of length a = 20 nm. The bending energy (Y. Wang et al., 2011) associated with the chain is defined

as $\frac{1}{k_B T} U_{bend} = \kappa \sum_{j=1}^{N-1} 1 - \cos\theta_j$, where k is the prefactor defined as $k = l_K / a$. The excluded volume effect is implemented as hard sphere potential energy between close beads $\frac{1}{k_B T} U_{EV}(i, j) = \infty$ when the distance between any two beads becomes closer than w (Tree, Wang, & Dorfman, 2013). The potential energy is considered 0 as distance exceeds w. The cutoff distance w is defined as the bead width and is given by $w = a/2^{1/6}$ = 17 nm. In the simulation of DNA migration in nanoslits, we tested four different DNA fragments, N = 600, 800, 1000, 1200 and in the free energy analysis using biased Rosenbluth sampling only the fragment N = 800 is chosen as target molecule (the contour length of the fragment N = 800 is 16 μm which is close to lambda DNA).

6.2.3 Biased Rosenbluth Sampling

The main steps of Biased Rosenbluh sampling are the same as Prune-Enriched Rosenbluth sampling except that during each chain-growing step there is no prune or enrich process. Generally, the first bead is placed in the channel with x coordinate randomly distributed in [1500 2500] (see structure of nanofilter in **Figure 27**), which will ensure the grown chain will gather around the entrance of constriction area. At this time the Rosenbluth factor of the chain is 1. Then in order to add new bead, we first generate K trial configurations according to the distribution described in previous chapter. For each configuration, we calculate the introduced excluded volume potential and electrostatic potential according to the external field and generate a scaling parameter based on the added total energy of the trail new bead reads as,

$$w_l(i) = \exp[-(U_E(i) + \sum_{j=1}^{j=i-1} U_{EV}(i,j))/k_BT] \quad (29)$$

l = 1, 2, … K and i denotes the i^{th} bead to add to the chain. Among these trial configurations one is randomly chosen based on its probability y $p(l) = w_l / \sum_{l=1}^{l=K} w_l$ and the Rosenbluth factor updates as $W(i) = W(i-1)w_l(i)/K$. After the whole is grown, we could estimate the excess free energy U of the chain as reference to free chain in absence of external field $W_{chain} = \exp(-U/k_BT)$.

6.3 Results and Discussion

6.3.1 Activation Time and Activation Energy Model

The mobility of DNA migrating through nanofilters (J. Y. Han & Craighead, 2002) follows equation: $\frac{\mu}{\mu_0} = \frac{\tau_{mig}}{\tau_{mig} + \tau_{trap}}$, where μ_0 is the DNA free solution mobility in free space. $\tau_{mig} = 2L_0/\mu_0 E_{ave}$ is the time DNA used to migrate unit length L if there is no constriction in the channel, and τ_{trap} is defined as extra time DNA needed to overcome energy barrier and squeeze into shallow region in channel. E_{ave} is the average electric field strength calculated from the periodic boundary condition, $E_{ave} = V_0/2L_0$. In the simulation, we first run DNA migration in free space in order to get the free solution mobility μ_0. Then for the migration in the nanofilter we recorded the displacement of DNA's center of mass with certain frequency. Final velocity of DNA migration can be approached with a linear fit between the recorded time-versus-position data. Previously proposed activation models (Chen & Escobedo, 2003; Sakaue, 2006;

Wong & Muthukumar, 2008) assumed following scaling behavior for trap time: $\tau_{trap} = \tau_0 \exp\left(F_{act} / k_B T\right)$, in which τ_0 is electric field independent prefactor and F_{act} is the activation energy barrier associated with entry to the shallow space in the channel. The free energy landscape of DNA motion in such a scenario is affected by two factors. The first one is the confinement energy U_{conf}, from the segments DNA inserted into the shallow region. The second factor is the electrostatic energy U_E as DNA moves in external electric field. A possible scaling proposed by the activation model is that $U_{conf} \sim x$ and $U_E \sim -Ex^2$, where x denotes the number of segments DNA inserted inside the shallow part of the channel. This gives $F_{act} = \Delta U_{max} \sim 1/E$, which has been proven by many experiment and simulations. However, we noticed that all these studies focused on the cases where a relatively high electric field strength is applied. We postulate that in a low electric field, the scaling of the activation energy and thus the activation time could be different. At low electric fields, DNA molecules may no longer be aligned with the direction of electric field, therefore yielding a low dependence of U_E on x. Additinally, the confinement energy model probably needs refinement for the low electric field case. In order to first prove the idea of new scaling behavior of activation time versus electric field, we plot our simulated results from four different DNA molecules and notice an obvious shift as the electric field approaches values lower than 20 V/cm, the value below which is rarely studied in previous efforts. It is also clear in **Figure 28** that the previous scaling theory is recovered when the electric field strength is high enough.

6.3.2 Activation Model and Free Energy Landscape

In order to confirm the result from nanoslit transport simulations, we adopted the biased Rosenbluth sampling method to get the free energy distribution of DNA molecules, N = 800, with different molecular configurations inside the nanoslits under different electric field strength conditions. Our ensemble of DNA configurations also displayed different levels of penetration into the shallow region. As shown in **Figure 29**, the DNA free energy undergoes a local maximum that represents the extra energy necessary to overcome the entropic penalty associated with the constrictions. Similarly to the behavior we observed in the activation time scaling, we notice a transition of the scaling of activation energy on electric field strength. Both figures suggest that the existence of new behavior as DNA migrate in nanoslits driven by low electric field. To obtain a detailed understanding of the possible transport mechanism, we isolate each component of activation energy, U_{conf} and U_E, and find that each of them relates to electric field differently from the description in high electric field range.

The electrostatic energy is directly calculated as $U_E = \sum Q_i V_i$, where Q_i is the charge of each DNA segment and V_i is the potential at the segment center. To relate the U_E with electric field strength and penetration degree in the form $U_E \sim -Ex^k$ we found a gradual transition of k, plotted in **Figure 30**, from approximately 1.5 at low electric fields to 2.0 in the high electric field range. The confinement energy is acquired by subtracting the electrostatic energy from the free energy of the DNA molecule. The confinement energy shows a rapid increase (scales linearly with the penetration degree) as DNA first approaches and enters the slits. After some segments are inside the shallow

region, the increase of confinement energy gradually slows down (scales with the penetration degree following a power law), and finally the contribution from the confinement energy saturates. Combined with the initial analysis of free energy landscape, we see that at high electric fields the DNA molecules experience the local energy maximum at lower penetration degree, transforming to a linear scaling region in the confinement energy picture (solid red line in **Figure 31**). On the other hand, low electric fields will drag DNA molecules further into the shallow part to experience the local energy maximum and make the confinement energy less dependent on the penetration degree (dashed red line in **Figure 31**).

6.4 Summary

In this Chapter, we revisit the problem of transport of long DNA molecules in the channel with alternating deep wells and nanoslits (i.e., nanofilter). With the effort to study the activation behavior under weak electric field strength, we adopted a DNA model using segment length much smaller than the slit depth that is set to DNA Kuhn length. This model allows us to capture DNA sub Kuhn length behaviors. In the Monte Carlo simulation of DNA transport, we covered a full range of high to low electric field values. The activation times from this simulation exhibit transitional scaling with electric field when its strength becomes relatively weak. A further biased Rosenbluth sampling method enabled us to explore a large ensemble of DNA configurations inside the nanofilter, which could be used to approximate the DNA escape process according to different molecule penetration degrees. DNA molecules driven by higher electric fields

arrive at the transition state (maximum local free energy) by inserting fewer segments into the nanoslit while more segments are needed to enter the slit before successful escape when DNA molecule moves in weaker electric field. The entropic term in the free energy, confinement energy increases linearly with penetration degree during earlier stage and becomes to increase slower thereafter. The enthalpic term, electrostatic energy, scales with penetration degree to the power of 2 in high electric field and the power decreases gradually as the field becomes weaker. These two terms combined together contribute to the transitional scaling behavior of activation energy in the low electric field region.

CHAPTER VII

CONCLUDING REMARKS

Although first introduced a decade ago, the unusual macromolecular transport phenomena, *entropic trapping*, has not received much attention until recently as microfabricated devices have become available such as nanoslit arrays that are able to mimic a confining environment close to molecule size scales. But a major shortcoming of this free solution electrophoresis approach to study entropic trapping lies in fabrication limits associated with constructing synthetic structures incorporating the necessary nanoscale dimensions. We instead adapted conventional polyacrylamide-based gel electrophoresis in a microchip format, which allow us to incorporate both the advantages of the microchip platform like fast operation and accurate data collection so that we can explore the macromolecular transport physics in these more complex nano-porous surroundings.

We have developed a new transport model to describe this process and develop an improved understanding of the fundamental physics. Based our ability to characterize the gel pore morphology, we successfully incorporate this distribution into the transport model. As shown in Chapter III, the transport model we proposed is able to connect various conditions with DNA electrophoretic transport modes using a phase diagram construction. We clearly show that the ratio of activation time to free migration time is the key parameter to determine the level of entropic trapping, although only activation time is intuitively related to the process to compensate for local entropic energy penalty.

More importantly, we reveal a promising feature of entropic trapping transport mode characterized by increasing separation resolution with DNA fragment length.

Despite the potential to be applied as new separation technique, entropic trapping transport still exhibits high diffusion due to the random thermal motion in the activation process which is an intrinsic behavior of entropic trapping. In Chapter IV we introduce an approach to solve these issues following a counter-intuitive approach. Normally, in order to improve the system performance the generated noise should be suppressed to achieve a high signal to noise ratio. However, with the idea of stochastic resonance, we are able to globally synchronize the discrete and noise-generation hopping events in entropic trapping with an external oscillating driving force whose period is tuned to match the average hopping rate. We emphasize that our method adopted the form of pulsed field electrophoresis that is different from previous experiments in that we are trying to use pulsed fields to regulate molecular level events. Besides improving the separation performance by reducing the time variation of the hopping events, we also observe a mobility maximum associated with the frequency of the pulsed field and molecular size. This resonance phenomenon enables us to introduce the idea of an entropic force microscope that probes molecular conformation via a simple microchip gel electrophoresis experiment. We have successfully applied this idea to discover two opposite binding effects of daunomycin and YOYO-1 with DNA.

In Chapters V and VI, two different computer simulation techniques are presented to study stochastic resonance and entropic trapping theoretically for short rigid and long DNA molecules in confining channels. A Brownian dynamics simulation is

used to study the Brownian particle transport behavior in channels with non-uniform cross-sections. By carefully tuning the magnitude and frequency of the driving force, we show that stochastic resonance is achieved where the movement of particle coincides with the driving force cycle. The study of stochastic resonance is also extended to channel with alternating constrictions, where we demonstrate a stable and selective particle trapping by delicately tuning the phase value of the periodic driving force in each section of the channel. In Chapter VI we adopt Monte Carlo simulation to refine the activation model previously proposed to describe the process of long DNA molecules squeeze into shallow region in nanofilters. DNA is modeled as series beads connected by rods of length 20 nm, which is much smaller than the depth in shallow channel and allows us to probe sub-Kuhn-length behavior of DNA molecules. A more accurate definition of penetration degree and study over broad range of applied electric field strengths reveal an overlooked regime in low electric field that is potentially helpful to design new separation techniques based on nanoslit arrays.

In the future, we believe there are several important techniques that could advance our current studies. First, our strategy to probe molecular conformation via entropic gel electrophoresis offers the possibility for large scale and parallel operations to obtain molecule size information. The successful design and fabrication of microdevice could finally lead to real application of our ideas in much easier way compared with other techniques mentioned in Chapter IV. Also it is highly desirable to adapt our ideas to the area of DNA-protein interactions that are usually important in biological activities.

The theoretical approach demonstrated in Chapter V also is appealing to develop real low power-consuming applications such as the isolation of cell collection, bacterial capsules isolation, and ionic transport, during which the targets would behave like Brownian particles. The main challenges for this application are the design and characterization of channel structure with alternating constrictions allowing easy manipulation of axial driving force as well as transverse constant force. Meanwhile, the assumptions we introduce to the previous proposed activation model need more experimental verification. An ideal case would be the realization of single molecule imaging during the activation process, in which we could build a profile of penetration degree, molecular conformation change, and different time scales in real time. These data could help us to further understand the entropic trapping behavior of long molecules and eventually lead to improved separation design.

REFERENCES

Ajdari, A., & Prost, J. (1991). Free Flow Electrophoresis with Trapping by a Transverse Inhomogeneous Field. *Proceedings of the National Academy of Sciences, 88*, 4468-4471.

Burada, P. S., Schmid, G., Reguera, D., Rubi, J. M., & Hänggi, P. (2009). Entropic Stochastic Resonance: the Constructive Role of the Unevenness. *The European Physical Journal B, 69*(1), 11-18.

Burada, P. S., Schmid, G., Reguera, D., Vainstein, M., Rubi, J., & Hänggi, P. (2008). Entropic Stochastic Resonance. *Physical Review Letters, 101*(13).

Chen, Z., & Escobedo, F. A. (2003). Simulation of Chain-Length Partitioning in a Microfabricated Channel via Entropic Trapping. *Molecular Simulation, 29*(6-7).

Craighead, H. G., Han, J., & Turner, S. W. (1999). Entropic Trapping and Escape of Long DNA Molecules at Submicro Size Constriction. *Physical Review Letter, 83*, 1688.

Cullinane, C., Cutts, S. M., Panousis, C., & Phillips, D. R. (2000). Interstrand Cross-linking by Adriamycin in Nuclear and Mitochondrial DNA of MCF-7 Cells. *Nucleic Acids Research, 28*, 1019-1025.

de Gennes, P. G. (1979). *Scaling Concepts in Polymer Physics*. Ithaca,NY: Cornell University Press.

Doi, M., & Edwards, S. F. (1986). *The Theory of Polymer Dynamics*. Oxford,UK: Oxford University Press.

Dorfman, K. (2010). DNA Electrophoresis in Microfabricated Devices. *Reviews of Modern Physics, 82*(4), 2903-2947.

Drougin, G., Slater, G. W., & Mayer, P. (1996). Migration of DNA Through Gels. *Methods in Enzymology, 270*.

Dubkov, A., & Spagnolo, B. (2005). Acceleration of Diffusion in Randomly Switching Potential with Supersymmetry. *Physical Review E, 72*(4).

Duke, T. A. J., Austin, R. H., Cox, E. C., & Chan, S. S. (1996). Pulsed-field Electrophoresis in Microlithographic Arrays. *Electrophoresis, 17*, 1075-1079.

Eckel, R., Ros, R., Ros, A., Wilking, S. D., Sewald, N., & Anselmetti, D. (2003). Identification of Binding Mechanisms in Single Molecule-DNA Complexes. *Biophysical Journal, 85*(3), 1968-1973.

Fiasconaro, A., & Spagnolo, B. (2011). Resonant Activation in Piecewise Linear Asymmetric Potentials. *Physical Review E, 83*(4).

Flory, P. J. (1953). *Principles of Polymer Chemistry*. Ithaca,NY: Cornell University Press.

Frenkel, D., & Smit, B. (2002). *Understanding Molecular Simulation from Algorithms to Applications*. New York: Academic Press.

Fu, J., Yoo, J., & Han, J. (2006). Molecular Sieving in Periodic Free-Energy Landscapes Created by Patterned Nanofilter Arrays. *Physical Review Letters, 97*(1).

Gammaitoni, L., Hanggi, P., Jung, P., & Marchesoni, F. (1998). Stochastic Resonance. *Reviews of Modern Physics, 79*, 223-287.

Gammaitoni, L., Marchesoni, F., Martinelli, M., Pardi, L., & Santucci, S. (1991). Phase Shifts in Bistable EPR Systems at Stochastic Resonance. *Physics Letters A, 158*, 449-452.

Giddings, J. C. (1991). *Unified Separation Science*. New York: Wiley.

Günther, K., Mertig, M., & Seidel, R. (2010). Mechanical and Structural Properties of YOYO-1 Complexed DNA. *Nucleic Acids Research, 38*, 6526-6532.

Han, J. (2000). Separation of Long DNA Molecules in a Microfabricated Entropic Trap Array. *Science, 288*(5468), 1026-1029.

Han, J. Y., & Craighead, H. G. (2002). Characterization and Optimization of an Entropic Trap for DNA Separation. *Analytical Chemistry, 74*.

Harms, Z. D., Mogensen, K. B., Nunes, P. S., Zhou, K., Hildenbrand, B. W., Mitra, I., . . . Jacobson, S. C. (2011). Nanofluidic Devices with Two Pores in Series for Resistive-Pulse Sensing of Single Virus Capsids. *Anal Chem, 83*(24), 9573-9578.

Hasegawa, Y., & Arita, M. (2012). Fluctuating Noise Drives Brownian Transport. *J R Soc Interface, 9*(77), 3554-3563.

Kasianowicz, J. J., Brandin, E., Branton, D., & Deamer, D. W. (1996). Characterization of Individual Polynuecleotide Molecules Using a Membrane Channel. *Proceedings of the National Academy of Sciences, 93*, 13770.

Kim, S. H., Panwar, A. S., Kumar, S., Ahn, K. H., & Lee, S. J. (2004). Electrophoresis of a Bead-Rod Chain Through a Narrow Slit: A Brownian Dynamics Study. *The Journal of Chemical Physics, 121*(18), 9116-9122.

Kramers, H. A. (1940). Brownian Motion in a Field of Force and the Diffusion Model of Chemical Reactions. *Physica, 7*, 284-304.

Lanzara, E. (1997). Experimental Study of a Nonlinear System in the Presence of Noise: the Stochastic Resonance. *American Journal of Physics, 65*(4), 341.

Lee, C. Y., Choi, W., Han, J. H., & Strano, M. S. (2010). Coherence Resonance in a Single-Walled Carbon Nanotube Ion Channel. *Science, 329*(5997), 1320-1324.

Liu, L., Li, P., & Asher, S. A. (1999). Entropic Trapping of Macromolecules by Mesoscopic Periodic Voids in a Polymer Hydrogel. *Nature, 397*, 141.

Lo, R. C., & Ugaz, V. M. (2008). Microchip DNA Electrophoresis with Automated Whole-gel Scanning Detection. *Lab Chip, 8*(12), 2135-2145.

Luckey, J. A., Norris, T. B., & Smith, L. M. (1993). Analysis of Resolution in DNA Sequencing by Capillary Gel Electrophoresis. *Journal of Chemical Physics, 97*(12).

Minc, N., Bokov, P., Zeldovich, K. B., Fütterer, C., Viovy, J. L., & Dorfman, K. D. (2005). Motion of Single Long DNA Molecules through Arrays of Magnetic Columns. *Electrophoresis, 26*(2), 362-375.

Minotti, G., Menna, P., Salvatorelli, E., Cairo, B., & Gianni, L. (2004). Anthracyclines: Molecular Advances and Pharmacologic Developments in Antitumor Activity and Cardiotoxicity. *Pharmacological Reviews, 56*, 185-299.

Nixon, G. I., & Slater, G. W. (1996). Entropic Trapping and Electrophoretic Drift of a Polyelectrolyte Down a Channel with a Periodically Oscillating Width. *Physical Review E, 53*.

Nkodo, A. E., Garnier, J. M., Tinland, B., Ren, H. G., Desruisseaux, C., McCormick, L., . . . Slater, G. W. (2001). Diffusionco Efficient of DNA Molecules during Free Solution Electrophoresis. *Electrophoresis, 22*.

Ogston, A. G. (1958). The Spaces in a Uniform Random Suspension of Fibres. *Transactions of the Faraday Society, 54*.

Olson, D. W., Ou, J., Tian, M., & Dorfman, K. D. (2011). Continuous-Time Random Walk Models of DNA Electrophoresis in a Post Array: Part I. Evaluation of Existing Models. *Electrophoresis, 32*, 573-580.

Ou, J., Cho, J., Olson, D. W., & Dorfman, K. D. (2009). DNA Electrophoresis in a Sparse Ordered Post Array. *Physical Review E, 79*(6), 4.

Panwar, A. S., & Kumar, S. (2006). Time Scales in Polymer Electrophoresis through Narrow Constrictions: a Brownian Dynamics Study. *Macromolecules, 39*(3), 1279-1289.

Pizzolato, N., Fiasconaro, A., Adorno, D. P., & Spagnolo, B. (2013). Translocation Dynamics of a Short Polymer Driven by an Oscillating Force. *J Chem Phys, 138*(5), 054902.

Prellberg, T., & Krawczyk, J. (2004). Flat Histogram Version of the Pruned and Enriched Rosenbluth Method. *Physical Review Letters, 92*.

Reguera, D., Schmid, G., Burada, P., Rubí, J., Reimann, P., & Hänggi, P. (2006). Entropic Transport: Kinetics, Scaling, and Control Mechanisms. *Physical Review Letters, 96*(13), 130603.

Rhee, K. W., & Ware, B. R. (1983). DNA–Divalent Metal Cation Interactions Measured by Electrophoretic Light Scattering. *Journal of Chemical Physics, 78*, 3349-3353.

Rousseau, J., Drougin, G., & Slater, G. W. (1997). Entropic Trapping of DNA during Gel Electrophoresis Effects of Field Intensity and Gel Concentrations. *Physical Review Letter, 79*, 1945.

Sakaue, T. (2006). DNA Electrophoresis in Designed Channels. *The EuropeanPhysical Journal E, 19*(4).

Sebastian, K. L., & Paul, A. K. R. (2000). Kramers Problems for a Polymer in a Double Well. *Physical Review E, 62*, 927.

Shaikh, F. A., & Ugaz, V. M. (2006). Collection, Focusing, and Metering of DNA in Microchannels Using Addressable Electrode Arrays for Portable Low-power Bioanalysis. *Proc Natl Acad Sci U S A, 103*(13), 4825-4830.

Shi, N., & Ugaz, V. M. (2010). Tailoring the Nanoporous Architecture of Hydrogels to Exploit Entropic Trapping. *Physical Review Letters, 108*, 108101.

Sischka, A., Toensing, K., Eckel, R., Wilking, S. D., Sewald, N., Ros, R., & Anselmetti, D. (2005). Molecular Mechanisms and Kinetics between DNA and DNA Binding Ligands. *Biophys J, 88*(1), 404-411.

Slater, G. W., Desruisseaux, C., Hubert, S. J., Mercier, J. F., Labrie, J., Boileau, J., . . . Pepin, M. P. (2000). Theory of DNA Electrophoresis: A Look at Some Current Challenges. *Electrophoresis, 21*(18).

Slater, G. W., Kenward, M., McCormick, L. C., & Gauthier, M. G. (2003). The Theory of DNA Separation by Capillary Electrophoresis. *Current Opinion in Biotechnology, 14*.

Smisek, D. L., & Hoagland, D. A. (1990). Electrophoresis of Flexible Macromolecules Evidence for a New Mode Of Transport in Gels. *Science, 248*, 1221.

Spagnolo, B., & Mantegna, R. N. (1995). Stochastic Resonance in a Tunnel Diode in the Presence of White or Coloured Noise. *Nuovo Cimento, 17*.

Stockmayer, W. H. (1976). *Molecular Fluids*. In R. Balian & G. Weill (Eds.). London: Gordon and Breach.

Tessier, F., & Slater, G. W. (2002). Strategies for the Separation of Polyelectrolytes Based on Non-Linear Dynamics and Entropic Ratchets in a Simple Microfluidic Device. *Applied Physics A, 75*, 285-291.

Thomas, J. D. P., Joswiak, M. N., Olson, D. W., Park, S.-G., & Dorfman, K. D. (2013). Ratchet nanofiltration of DNA. *Lab on a Chip, 13*, 3741-3746.

Tree, D. R., Muralidhar, A., Doyle, P. S., & Dorfman, K. D. (2013). Is DNA a Good Model Polymer? *Macromolecules, 46*.

Tree, D. R., Wang, Y., & Dorfman, K. D. (2013). Extension of DNA in a Nanochannel as a Rod-to-Coil Transition. *Physical Review Letters, 110*.

van Dorp, S., Keyser, U. F., Dekker, N. H., Dekker, C., & Lemay, S. G. (2009). Origin of the Electrophoretic Force on DNA in Solid-state Nanopores. *Nature Physics, 5*.

Viovy, J. L. (2000). Electrophoresis of DNA and Other Polyelectrolytes: Physical Mechanisms. *Reviews of Modern Physics, 72*, 813.

Wang, J., Gonzalez, A. D., & Ugaz, V. M. (2008). Tailoring Bulk Transport in Hydrogels through Control of Polydispersity in the Nanoscale Pore Size Distribution. *Advanced Materials, 20*(23), 4482-4489.

Wang, Y., Tree, D. R., & Dorfman, K. D. (2011). Simulation of DNA Extension in Nanochannels. *Macromolecules, 44*.

Wong, A., & Muthukumar, M. (2008). Scaling Theory of Polymer Translocation into Confined Regions. *Biophysical Journal, 95*(8).

Zeman, S. M., Phillips, D. R., & Crothers, D. M. (1998). Characterization of Covalent Adriamycin-DNA Adducts. *Proc Natl Acad Sci U S A, 95*, 11561-11565.

Zhou, T., Moss, F., & Jung, P. (1990). Escape-time Distributions of a Periodically Modulated Bistable System with Noise. *Physical Review A, 42*, 3161-3169.

APPENDIX

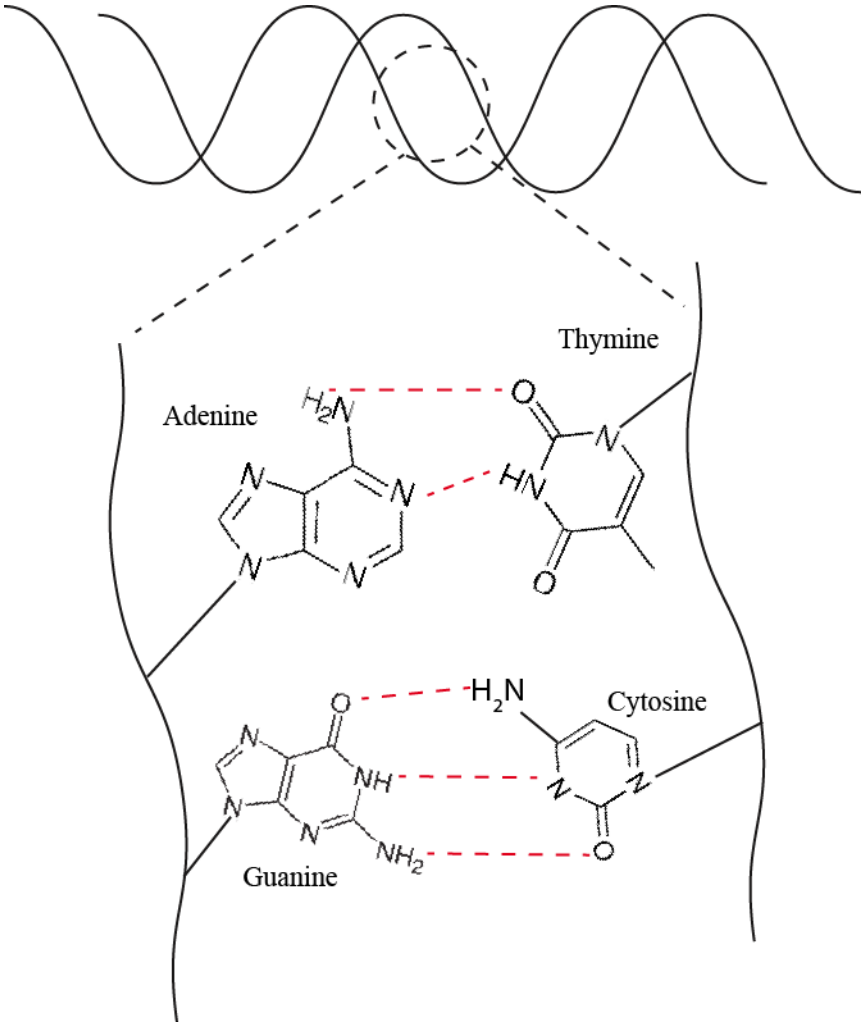

Figure 1 Schematic illustration of the double helix structure.
The two strands of DNA entwine to form the double helix structure and each strand is consisted of repeat unit of nucleotide. Each nucleotide contains the phosphate deoxyribose as the backbone and attached nucleobase to interact with nucleobase in the other strand. There are four kinds of nucleobases forming two pairing groups via hydrogen bonds (shown as red dashed lines in the figure).

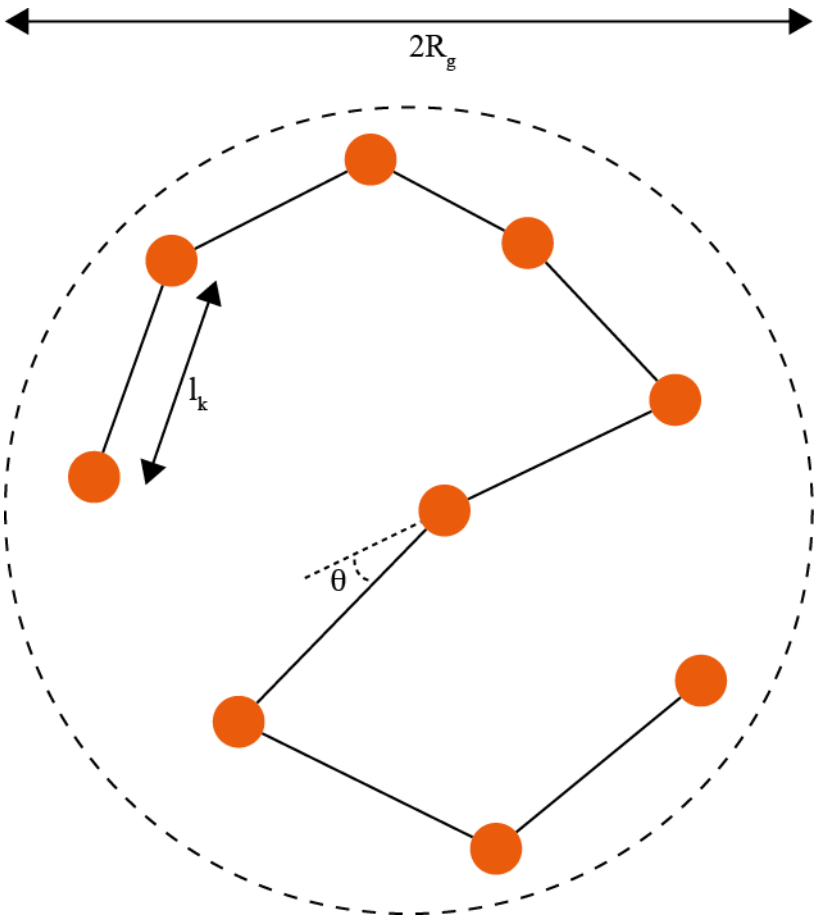

Figure 2 Corse grained model of DNA.
DNA is viewed in a length scale longer than the distance between adjacent nucleobases (0.34 nm), usually several Kuhn segment length. At this length scale adjacent chain segment is considered freely jointed with no energy associated with the bending angle θ denoted in the figure. DNA molecule will try to maximize the entropy (therefore minimize energy) to form a random coil configuration. The statistical size of the coil R_g can be scaled with the segment number and connecting bond length via the Flory exponent ν in the form $R_g^2 \sim l_K N_K^{2\upsilon}$, where υ takes the value of 0.5 in good solvent.

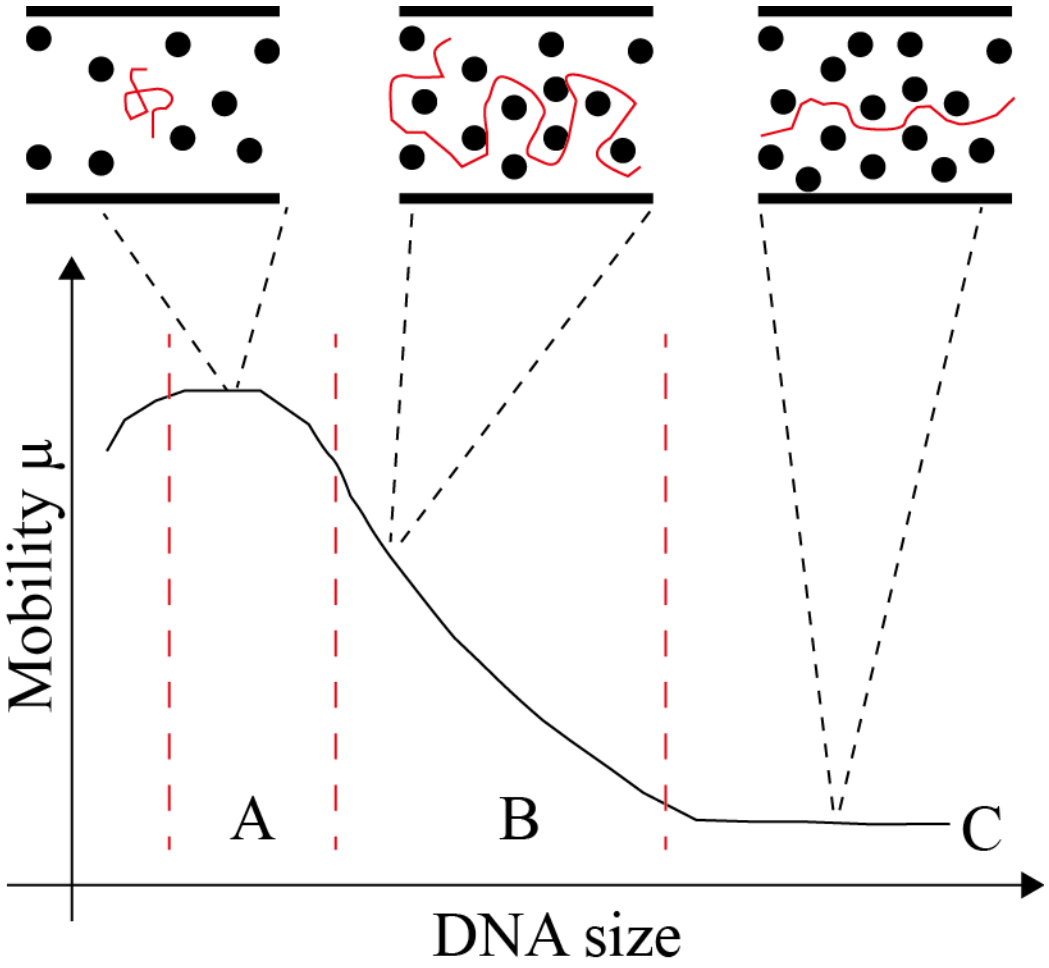

Figure 3 DNA adopts different migration modes in gel electrophoresis.
Based on the relative size of DNA and the free space in gel, there are roughly three common migration modes DNA will take. Regime A represents the case when DNA size is much smaller than the pore size and the observed mobility decays exponentially with DNA size. Regime B denotes the reptation regime where DNA size is much larger than free space in gel so it has to form curved shape to reptate through gel free space. As DNA size continues grows DNA molecule will aligned with the applied electric field. Shown in regime C, DNA molecules migrating in this mode cannot be separated on length. The black dots in the enlarged figures are representing the gel fibrils that can interact with DNA chain.

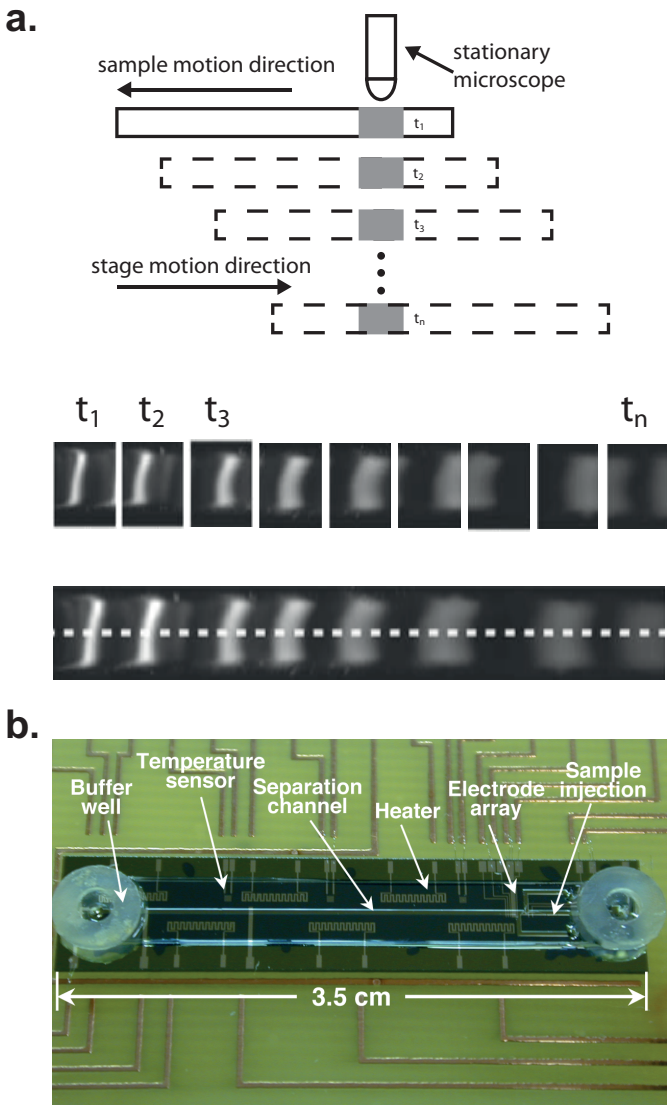

Figure 4 Experiment setup.
(a) Overview of the image collection and analysis procedures using whole channel scanning method. In each scan, a motorized stage carrying microchip enables a sequence of snapshots to be taken by a CCD camera interfaced with a fluorescence microscope. These individual snapshots are then assembled into a single composite image depicting all migrating DNA in the separation channel. A trace of fluorescence intensity versus position along the microchannel centerline is then extracted for computation of mobility and diffusion coefficients. (b) Top view of an assembled electrophoresis microchip. The cross-sectional dimensions of all channels are 275 (width) × 45 (height) μm. An electrode array is patterned on the silicon substrate (the "floor" of the microchannel) to enable on-chip collection and focusing of DNA samples. The microchips are mounted on printed circuit boards that allow the on-chip electrodes to be individually addressed after wire bonding.

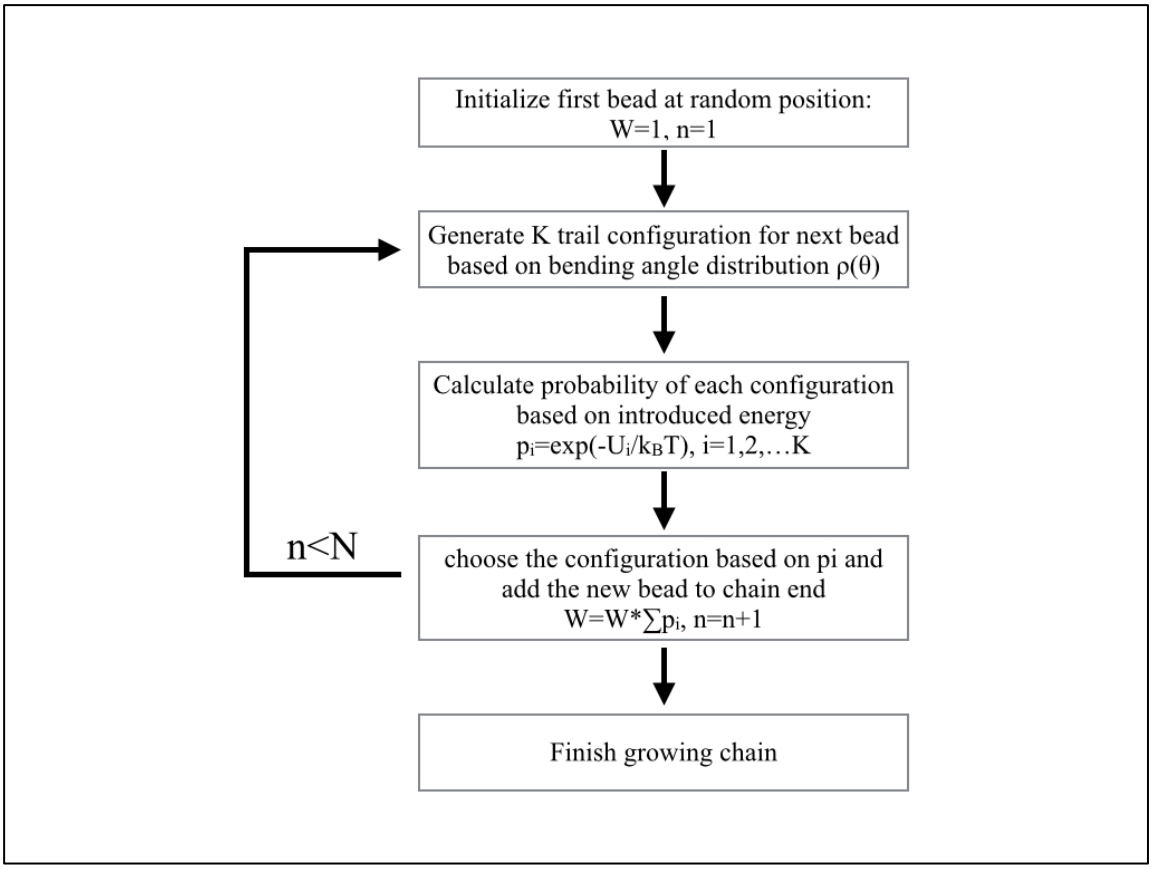

Figure 5 Flow Chart of standard biased Rosenbluth sampling method.
Polymer is consisted of *N* beads with *N*-1 connecting rods. During each cycle one bead is added to the chain end until the total length reaches the size of the polymer. There is a Rosenbluth factor associated with every growing chain. The described algorithm is paralleled independently for large amount of chain configurations.

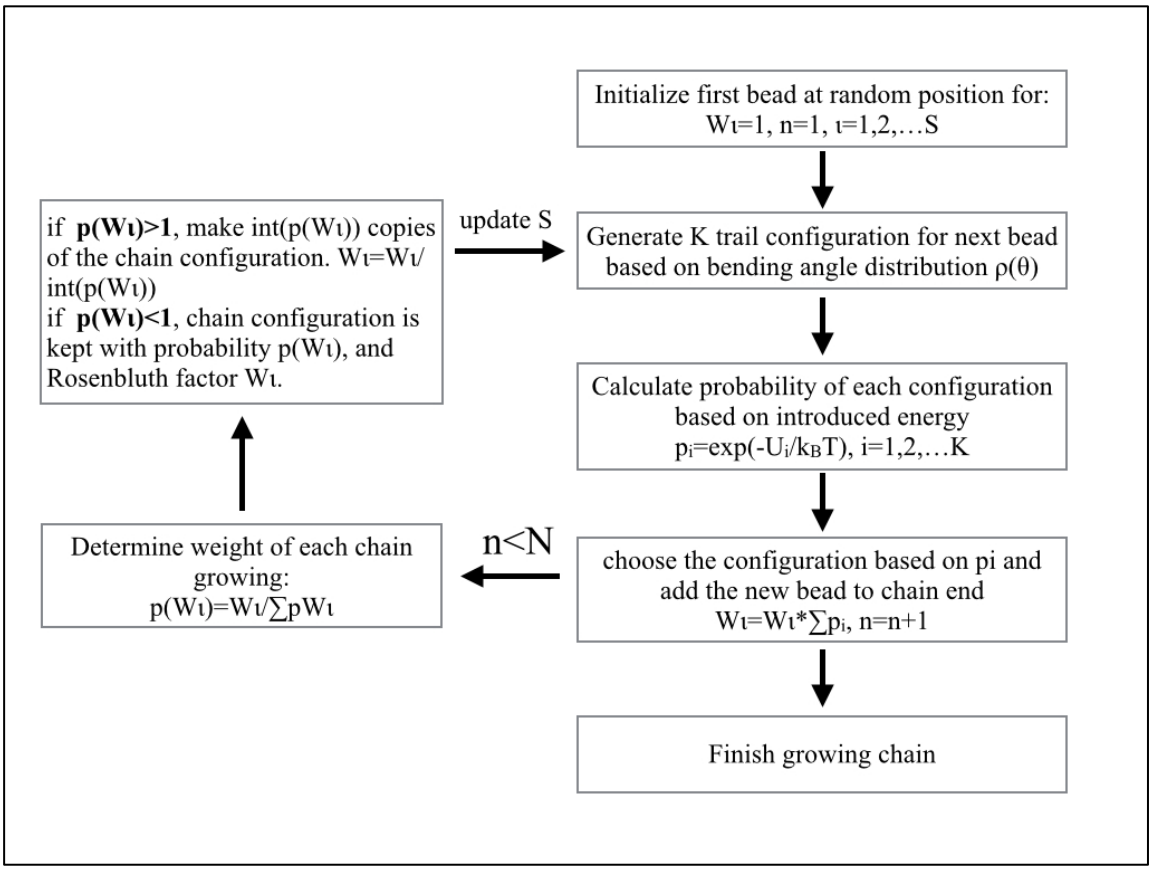

Figure 6 Flow Chart of standard PERM sampling method.
Extra step is taken after each bead is added to the chain end in PERM compared with Rosenbluth method. During simulation, large amount of chain configurations are sampled simultaneously and each chain configuration is enriched or pruned based on the weighted chain Rosenbluth factor. The basic idea behind the PERM is to make more copies of chain with larger Rosenbluth factor and delete chain with smaller Rosenbluth factor so that all the chain configurations in the ensemble have homogeneously distributed Rosenbluth factor.

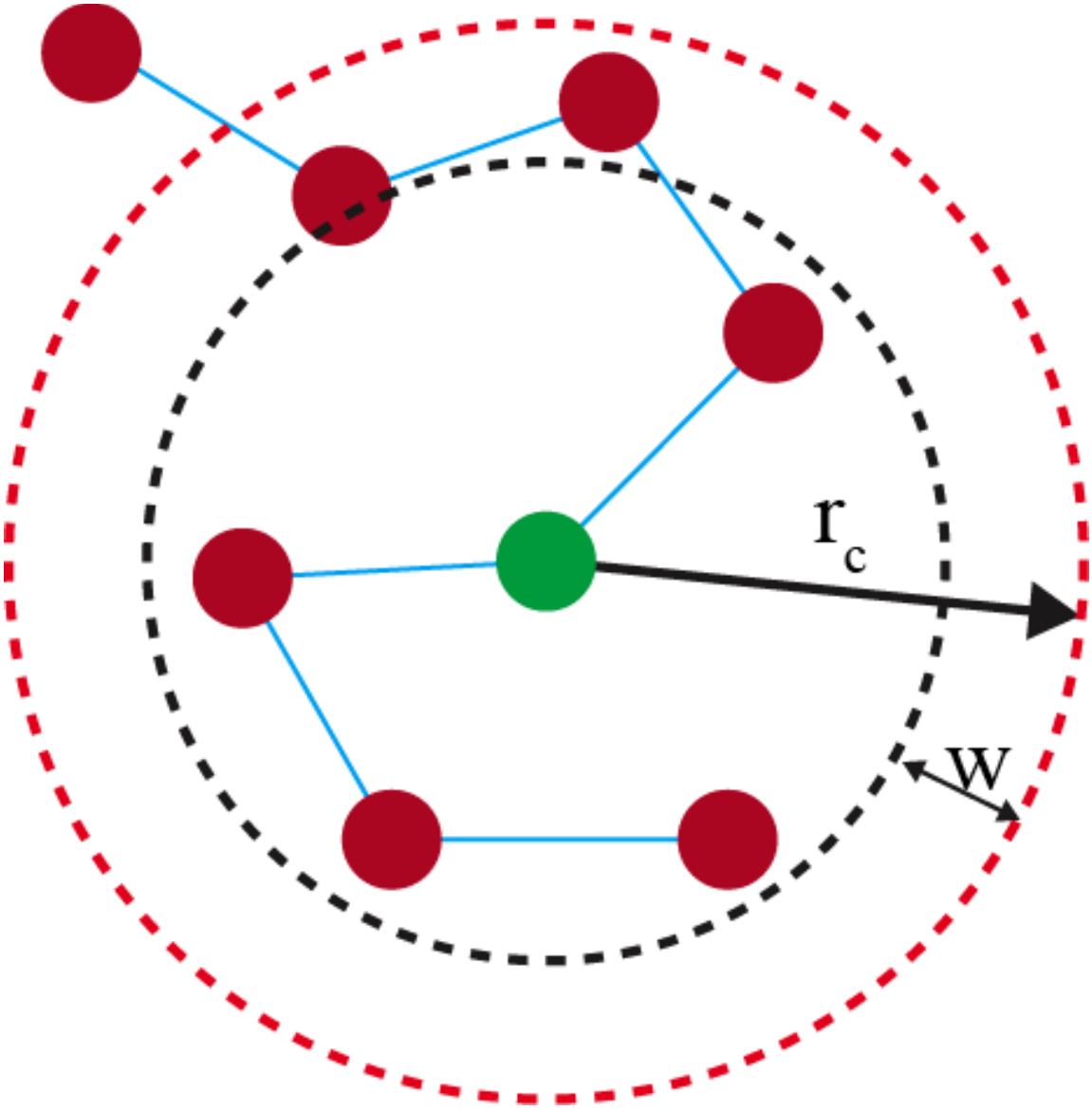

Figure 7 Verlet list is used to determine excluded volume effect.
At beginning, the first bead is centered at a sphere of radius r_c. As more beads are added to the chain, if the distance between new bead and the centered bead is smaller than r_c-w, the new bead is added the neighbor list (beads placed within the red dashed circle in the figure). For any new bead we only need to check its distance with the existing beads from the neighbor list. On the other hand, once a new bead exceeds the r_c-w radius (black dashed circle), it is then centered at a sphere of radius r_c and the neighbor list is recalculated.

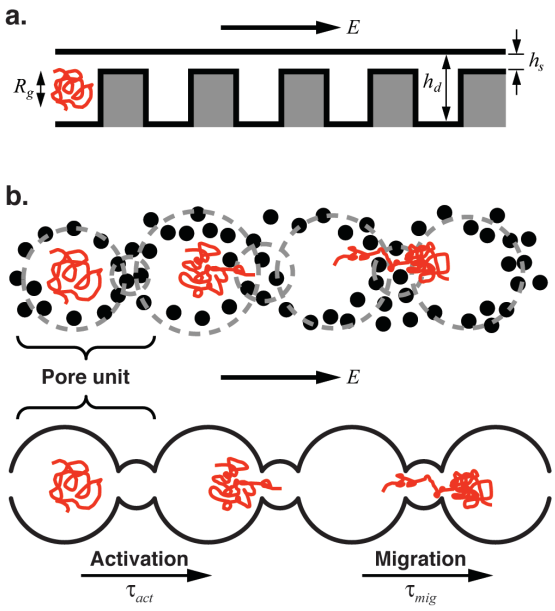

Figure 8 Electrophoretic transport of DNA by entropic trapping.
(a) "Nanofilters" are constructed from nanomachined structures designed to create a migration path consisting of alternating deep wells ($h_d \sim R_g$) and narrow slits ($h_s < R_g$). The idealized 2-D geometry is straightforward to model because it is describable solely in terms of these two length scales. (b) We model ET-dominated transport in hydrogels by representing the network as a randomly distributed ensemble of loosely and densely crosslinked regions (dots represent the gel fibrils, drawing is not to scale). DNA migration path can then be envisioned as a sequence of alternating large and small pores (i.e., a pseudo-nanofilter) of independently variable size.

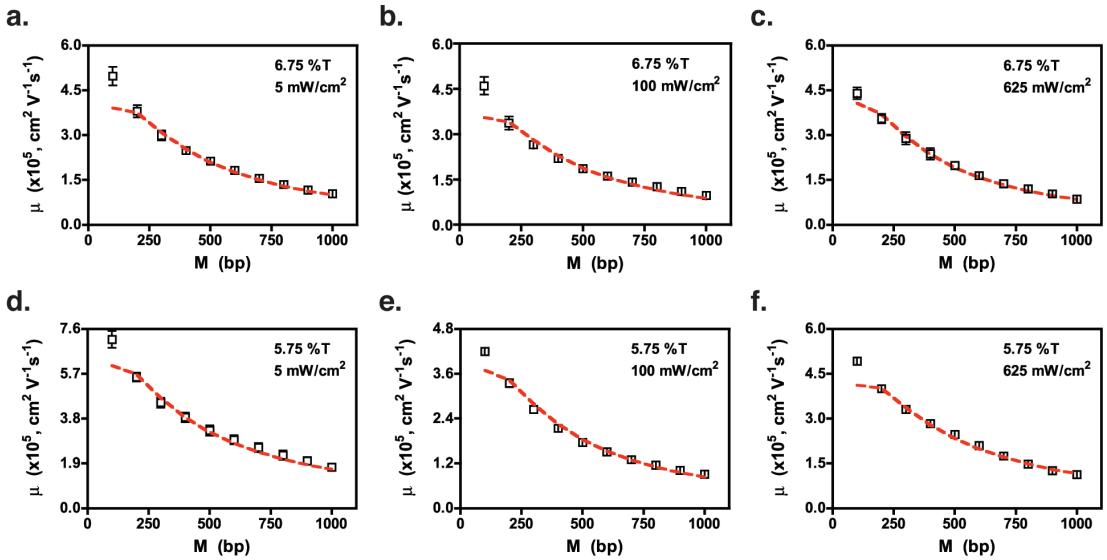

Figure 9 Transport model captures the size-dependence of double-stranded DNA electrophoretic mobility in hydrogels.
Data from microchip-based electrophoresis of a double-stranded DNA ladder are fit using Eq. (8) assuming a cylindrical pore geometry (C_2 = 0.85 [$nm^{1/\nu} \cdot bp^{-1}$]), leaving the constant C_4 as the only adjustable parameter. Despite the model's relative simplicity, all mobility data shown are fit remarkably well using a single value of $C_4 = 2.557 \times 10^5$ [$(bp^{1+\nu}) \cdot (V/cm)$]. The pore morphology was varied by adjusting the UV intensity applied to polymerize photocurable crosslinked polyacrylamide gels at concentrations of 6.75 %T (a-c) and 5.75 %T (d-f). Parameters associated with the average pore size and pore size distribution of each gel matrix are listed in Table S1. Error bars denote the standard deviation over an ensemble of 3 experiments.

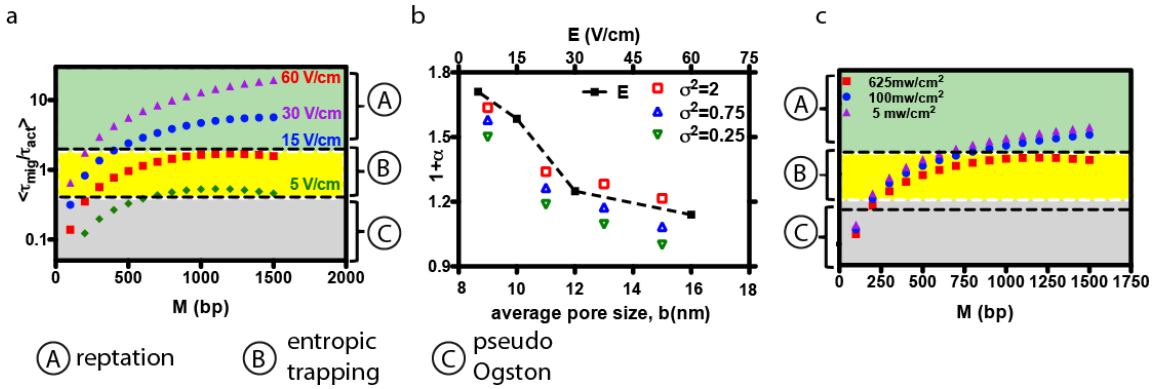

Figure 10 Relative influence of activation and migration timescales determines the predominant DNA migration mechanism in gel electrophoresis.
(a) The effect of electric field strength is plotted in a phase diagram, evaluated considering a 6.75 %T crosslinked polyacrylamide hydrogel (9 nm average pore size, 0.25 nm^2 variance). The ET-dominated regime is approximately defined between $0.5 < \tau_{mig}/\tau_{act} < 2$ (i.e., centered about $\tau_{mig}/\tau_{act} = 1$ on the log-scale plot). (b) Evolution of the size dependent mobility scaling $\mu \sim M^{-(1+a)}$ with electric field strength (upper abscissa) and average gel pore size (lower abscissa; E = 15 V/cm), indicating a transition to reptation-dominated transport ($1+a$ = 1 corresponds to reptation; 6.75 %T gel composition). Experimental data obtained under conditions where DNA migration was ET-dominated (E = 15 V/cm. 9 nm average pore size, 0.25 nm^2 variance) yielded $1+a$ = 1.51, corresponding to $\tau_{mig}/\tau_{act} \sim 2$. This was chosen to indicate a boundary between the ET and reptation in (a). (c) Of the three hydrogels considered with identical composition (6.75 %T) and electric field (15 V/cm), the gel cured at a UV intensity of 625 mW/cm^2 displays behavior most closely associated with the ET regimes.

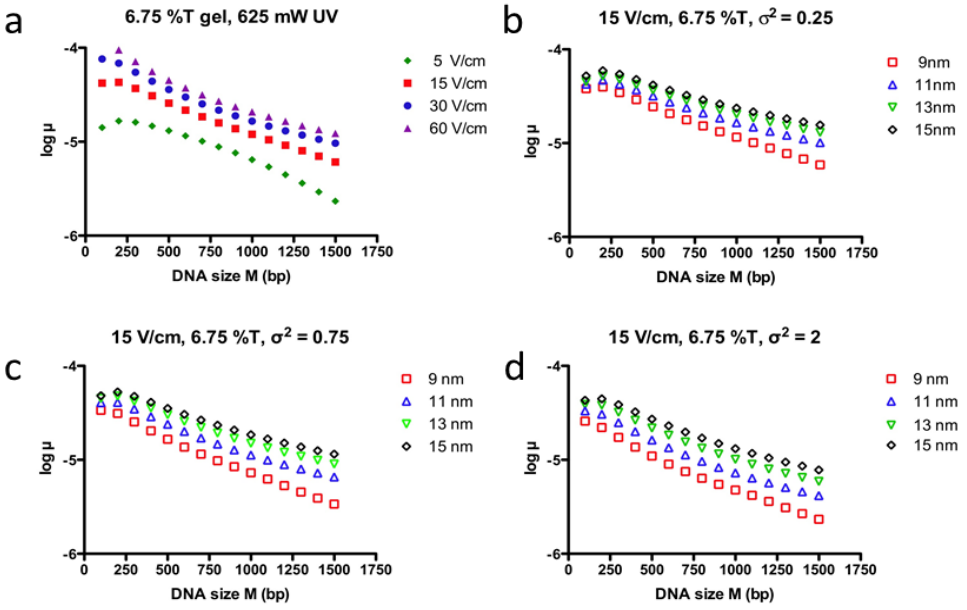

Figure 11 Evolution of mobility size dependence for 6.75 %T hydrogel.
(a) Influence of applied electric field. (b-d) Influence of gel average pore size for three different breadths of the pore size distribution (expressed in terms of the Gaussian variance σ^2). The slopes of these curves (in the range of linear dependence) are plotted in Figure 10-b extracting the scaling exponent 1 + *a*.

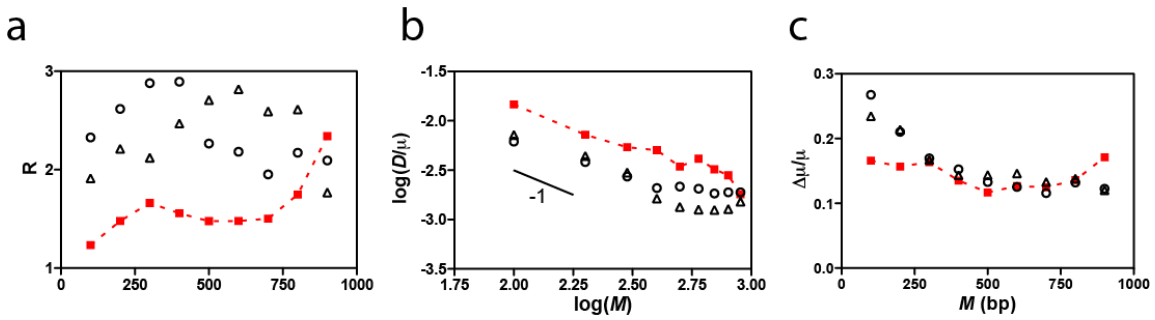

Figure 12 Unique characteristics of ET-dominated transport can be exploited to achieve improved separation performance.
(a) A gel formulation where migration is most strongly influenced by ET as determined from Figure 10-c (■, cured at a UV intensity of 625 mW/cm^2) displays an anomalous trend of separation resolution that increases with DNA size, especially at fragment lengths > 500 bp. In contrast, gel formulations where migration is dominated by reptation (cured at △ 5, and ○ 100 mW/cm^2) yield a more conventional trend of constant or decreasing resolution. A 1 cm separation length is assumed. (b) ET effects are evident in the size dependence of D/μ which decreases continuously over the entire DNA size range only in the gel displaying ET-dominated migration (symbols are the same as in (a)). The data also indicate that the Einstein relationship appears to be valid only in the 100 ~ 300 bp size range (a line with slope –1 is shown for guidance). (c) ET-induced effects are also responsible for unusual behavior in the size dependence of $\Delta\mu/\mu$, passing through a minimum in the vicinity of 500 bp beyond which it increases with DNA length (symbols are the same as in (a)). Data points corresponding to ET-dominated migration are connected by dashed lines to guide the eye.

Gel conc. (%T)	UV curing intensity (mW/cm^2)	b (nm)	σ^2 (nm^2)
	5	16	2
6.75	100	12	0.75
	625	9	0.25
	5	20	2
5.75	100	14	1.75
	625	12	0.35

Table 1 Summary of gel pore size data.
This set of data is used as inputs to apply the transport model in Eq. (8) for prediction of size-dependent electrophoretic mobility as shown in Figure 11. These data were determined based on characterization studies of similar hydrogels (J. Wang et al., 2008) .

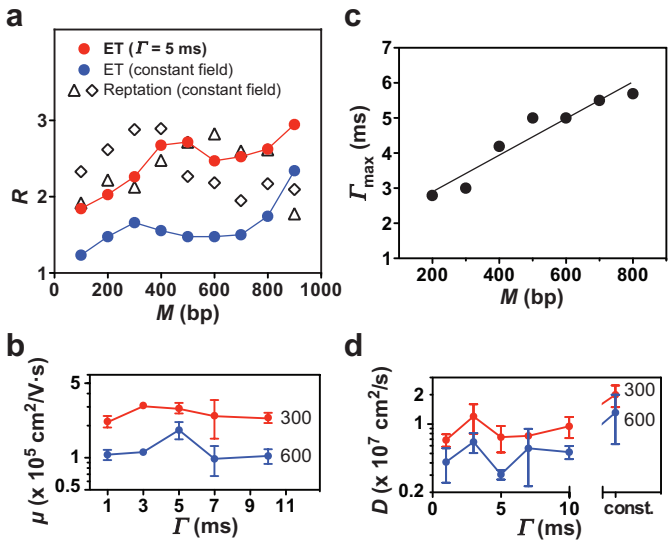

Figure 13 Electrophoretic migration in pulsed field shows improved performance and anomalous mobility behavior.
(a) Microchip gel electrophoresis of dsDNA in the ET regime (imposed by UV curing the gel matrix at 625 mW cm^{-2}) shows enhanced separation resolution under RET conditions when the electric field is cyclically switched on and off at Γ = 5 ms (●, red, E_{avg} = 15 V/cm; E_{avg} represents the time average electric field amplitude) versus application of a continuous field (●, blue, E = 15 V/cm). An inverted dependence of R on DNA size is also evident, as compared with the constant or decreasing size dependence of R in gels where transport is reptation-dominated (△, ◇; UV cured at 5 and 100 mW/cm^2 respectively, E = 15 V/cm). (b) Experimental measurements of mobility versus display a distinct peak in the vicinity of 5 ms that is most pronounced at DNA fragment lengths 500 bp and above. (c) Experimental data reveal that the actuation period associated with the mobility peak, Γ_{max}, is dependent on DNA fragment length (line denotes linear regression fit to the data). (d) The periodically applied electric field also yields a reduction in experimentally measured diffusion coefficients relative to the constant field case.

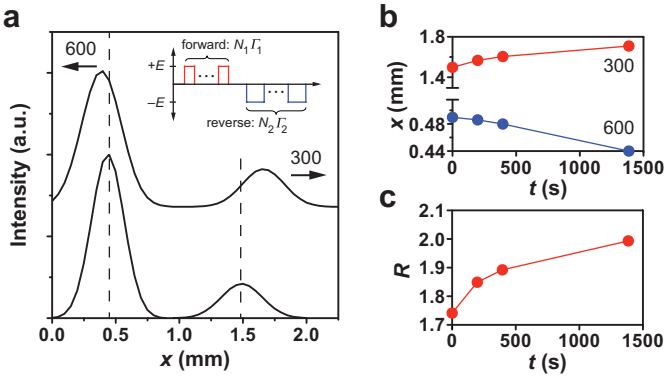

Figure 14 Bi-directional transport in gel electrophoresis under entropic trapping regime.
(a) A time sequence of intensity traces shows that bi-directional transport of 300 and 600 bp dsDNA fragments is achieved by applying alternating forward and backward pulses of an oscillatory electric field selected to optimize resonance in each species (1.1 min forward pulse at Γ_1 = 5 ms; 1.0 min backward pulse at Γ_2 = 2 ms; E_{avg} = 15 V/cm in both directions). The net result is (b) positive mobility of the leading species (μ_{300} = 1.5 x 10^{-5} cm^2 V^{-1} s^{-1}) and negative mobility of the trailing species (μ_{600} = –0.5 x 10^{-6} cm^2 V^{-1} s^{-1}), (c) yielding continually increasing separation resolution within a short distance. Intensity traces in (a) were acquired at t = 0 and 1400 s. Note that the electric field direction is only changed in the bi-directional transport cases shown in (a). Unidirectional fields are applied in all other experiments.

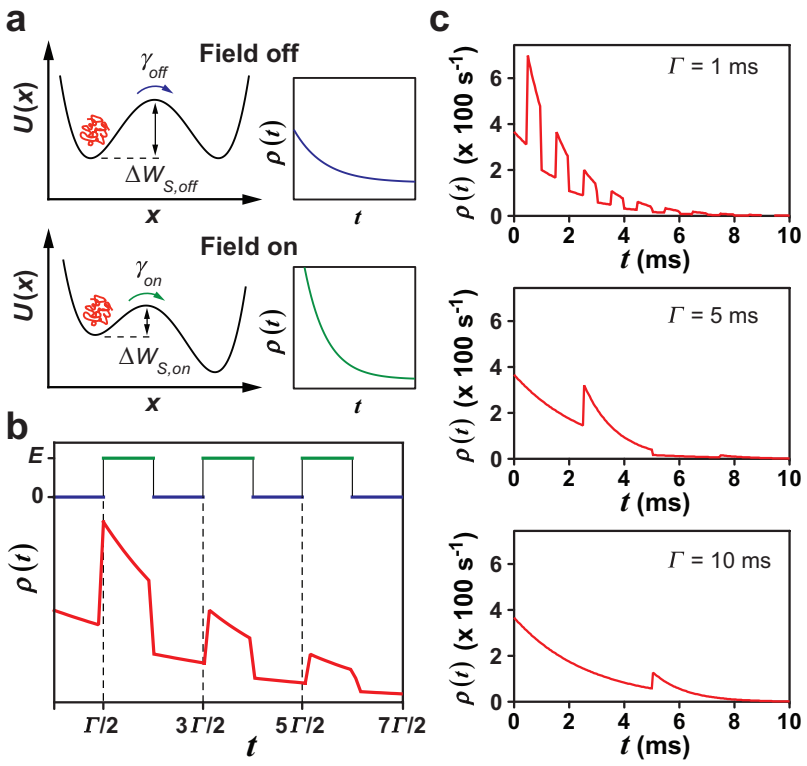

Figure 15 Trap time distribution entropic trapping with oscillating external electric field.

(a) The free-energy landscape $U(x)$ associated with electrophoretic DNA transport between neighboring gel pores is represented by a double potential well with an entropic energy barrier height ΔW_S and characteristic Kramers escape rate γ. In the absence of an applied electric field (top), the well displays a symmetric profile (Gammaitoni et al., 1998) with respect to x_m described by $\frac{U(x)}{4\Delta W_S} = -\frac{1}{2}\left(\frac{x}{x_m}\right)^2 + \frac{1}{4}\left(\frac{x}{x_m}\right)^4$, with barrier height $\Delta W_{S,off} = \Delta W_S$. The profile's symmetry is broken when an electric field is imposed (bottom), becoming tilted according to $\frac{U(x)}{4\Delta W_S} = -\frac{1}{2}\left(\frac{x}{x_m}\right)^2 + \frac{1}{4}\left(\frac{x}{x_m}\right)^4 - \left(\frac{F_{elec}x_m}{4\Delta W_S}\right)\frac{x}{x_m}$ with an accompanying decrease in barrier height to $\Delta W_{S,on} = \Delta W_S - F_{elec}\, x_m$ that also reduces the breadth of the activation time (residence time) distribution $\rho(t)$. (b) A periodically applied electric field causes $\rho(t)$ to alternate between the field-on and field-off states, yielding a distribution curve with peaks occurring at odd multiples of $\Gamma/2$. (c) The spacing between peaks relative to the overall breadth of the distribution can be tuned by adjusting the modulation period to achieve an optimal state of synchronization whereby the majority of pore-to-pore hops occur within a single field-on interval ($\Gamma \sim 5$ ms).

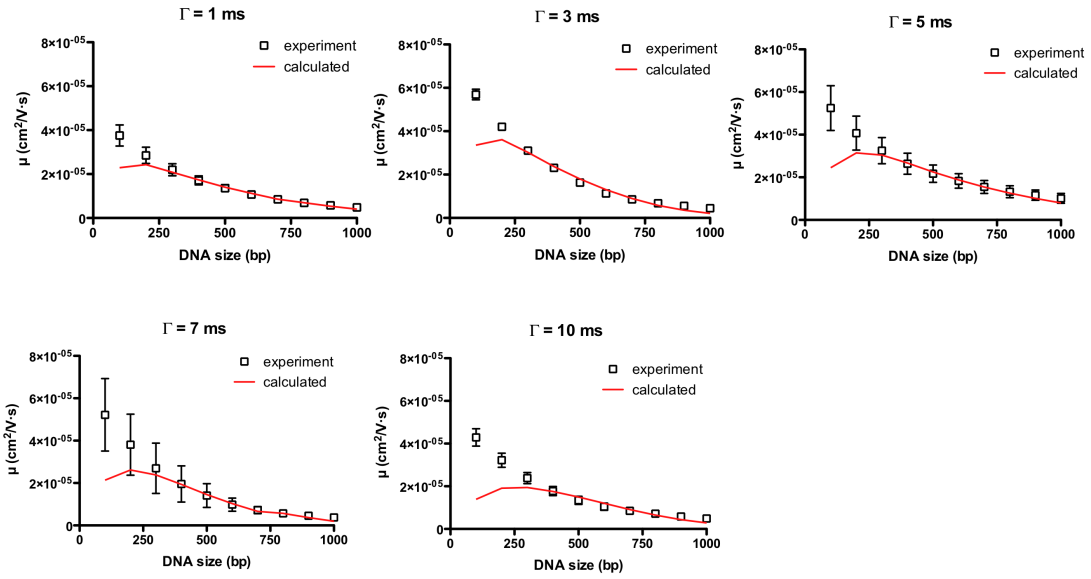

Figure 16 Fitting our transport model with microchip gel electrophoresis data. Our transport model captures the size-dependence of electrophoretic mobility under time varying electric fields over a range of actuation periods. Mobility data from microchip-based electrophoresis of a double-stranded DNA ladder were acquired at modulation period Γ ranging from 1 to 10 ms, and fit using Equation (6). The electric field amplitude was E_{on} = 15 V/cm, and the gel matrix was prepared by UV curing at 625 mW/cm^2. Error bars denote the standard deviation over an ensemble of 3 experiments.

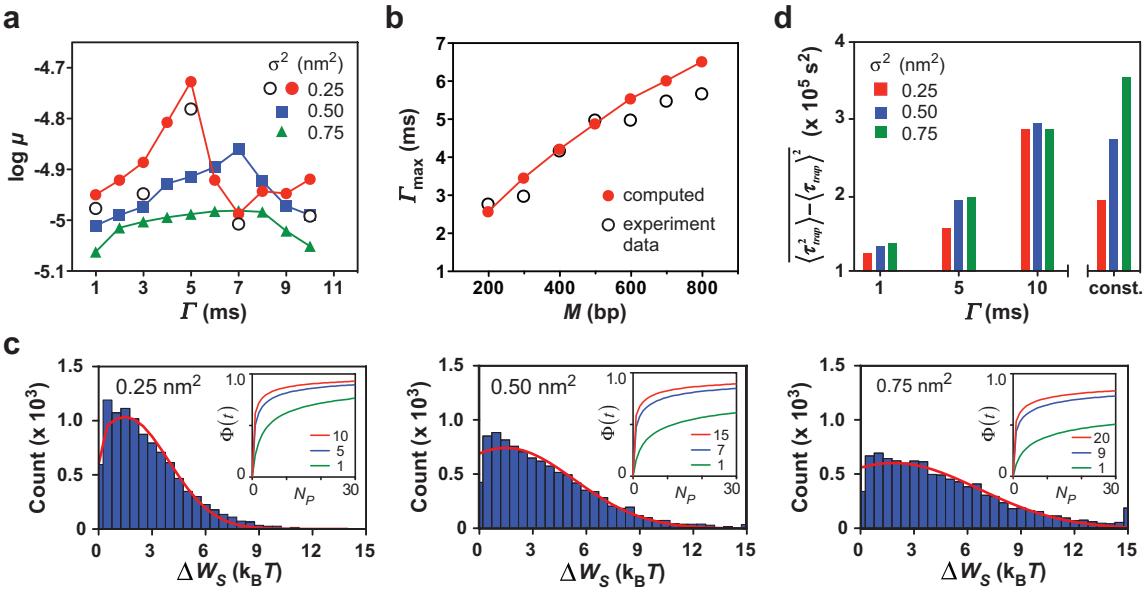

Figure 17 Explaining the experiment observations with our transport model. **(a) Predicted dependence of mobility on Γ for a 600 bp DNA fragment in hydrogel matrices incorporating three different pore size distribution breadths (expressed in terms of their Gaussian variance σ^2). The pronounced peak at $\Gamma = 5$ ms is evident at $\sigma^2 = 0.25$ nm^2, with good agreement between the predicted (filled symbols) and experiment (open symbols) values. The mobility peak shifts to higher Γ and decreases in height as the pore size distribution broadens. Stochastic resonance is evident in each case owing to the fact that $\gamma_{off}\Gamma/2 \sim 1$ is satisfied ($\gamma_{off}^{-1} = 3.2$, 4.3, and 5.2 ms for $\sigma^2 = 0.25$, 0.5, and 0.75 nm^2, respectively). (b) Comparison with experiment data in Fig. 2c shows that our transport model also predicts the DNA size dependence of the actuation period associated with the mobility peak, Γ_{max}. (c) Computed histograms of the entropic energy barrier height show a broadening of the distribution and increase in average value with increasing pore size polydispersity ($\Delta W_{S,avg} = 2.7$, 3.7, and 4.6 k_BT for $\sigma^2 = 0.25$, 0.5, and 0.75 nm^2, respectively). The insets show the predicted cumulative activation time probability $\Phi(t)$ versus the number of field actuation periods N_P at small (green), optimal (blue), and large (red) Γ (in units of ms). (d) Uncertainty in the trap time distribution yields a parameter proportional to the observed diffusion coefficient (overbar denotes integration over the pore size distribution). Predicted values are below the constant field condition in all cases, in agreement with experiment data in Figure 13.**

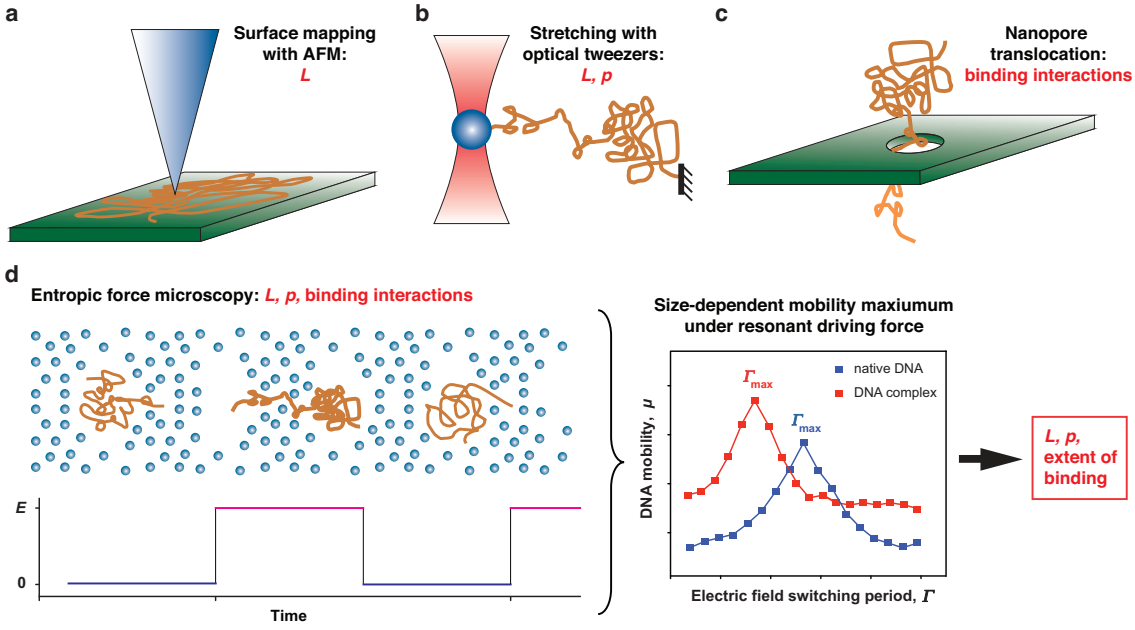

Figure 18 Overview of methods to quantitatively probe nanoscale macromolecular structure.
(a) Atomic force microscopy generates a 2D conformational map of macromolecules immobilized on a surface, from which the contour length (*L*) can be determined. (b) Stretching of a tethered macromolecule using optical tweezers enables both the contour length and persistence length (*p*) to be obtained from force vs. extension measurements, provided individual molecules are large enough to directly image. (c) Measurements of the blockade current during macromolecular translocation through nanopores enable binding interactions to be probed. (d) An entropic force microscope operates by monitoring the electrophoretic mobility of a macromolecular species in response to a periodic driving force (i.e., electric field switched on and off with period *Γ*). The surrounding nanoporous gel matrix (blue dots) incorporates a pore size distribution tailored such that transport occurs via entropic trapping, yielding a size-dependent mobility maximum under resonant electric field actuation conditions. This stochastic resonance state enables *L*, *p*, and the extent of binding to be simultaneously quantified. Macromolecules of arbitrary length can be probed, so long as the nanoporous surroundings are sized to enable entropic trapping transport.

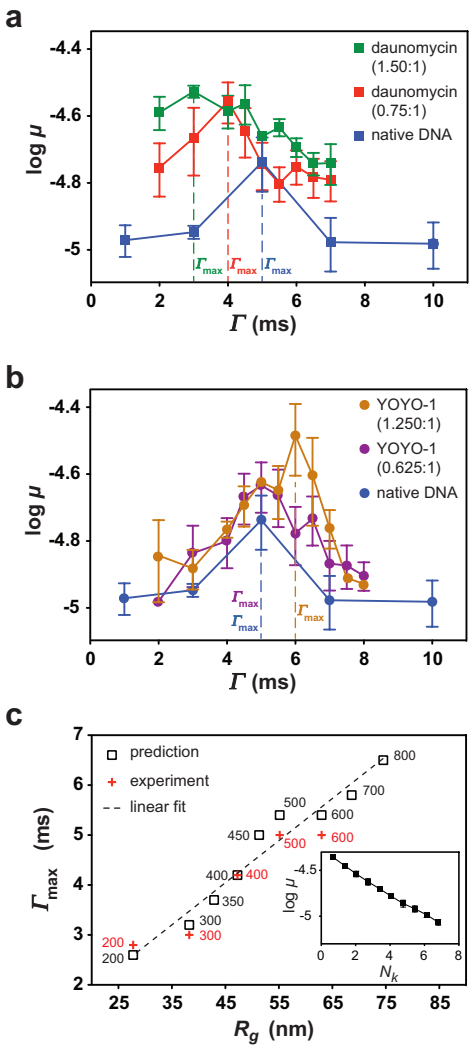

Figure 19 A size-dependent mobility peak emerges as a signature of resonant entropic transport.
(a) Effect of daunomycin binding on resonant entropic transport of 600 bp dsDNA confined in nanoporous surroundings. A shift in the resonant peak to lower electric field actuation periods is evident as the bound complex adopts a more compact conformation. (b) YOYO-1 interacts differently with DNA, displaying little conformational change at low concentrations and a shift in the resonant mobility peak to larger values at very high loadings indicative of a larger complex size. (c) Measurements of the resonant Γ_{max} over a range of native DNA fragments of known length enable the molecular size of the bound complex (R_g) to be determined. The experimentally determined relationship between μ and N_k for a native 100 bp dsDNA ladder obtained under a constant electric field is shown in the inset. All time-varying electric fields are applied such that E_{avg} = 15 V/cm, constant field experiments are performed at E = 15 V/cm.

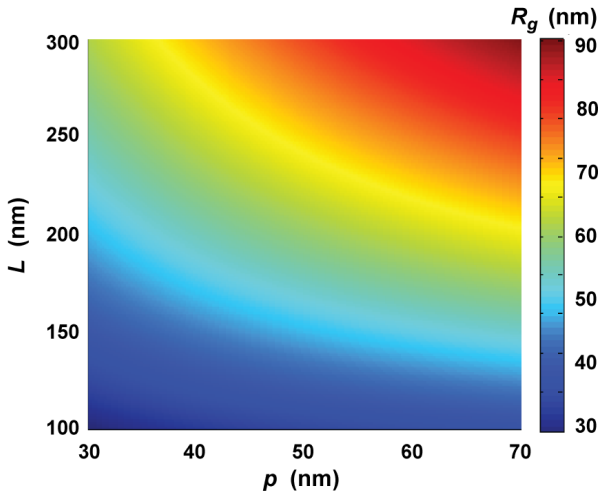

Figure 20 Parametric mapping of the Kratky-Porod equation.
The worm-like chain model's predicted interdependence between the contour length (L), persistence length (p) and radius of gyration (R_g) for dsDNA in the sub-1,000 bp size range.

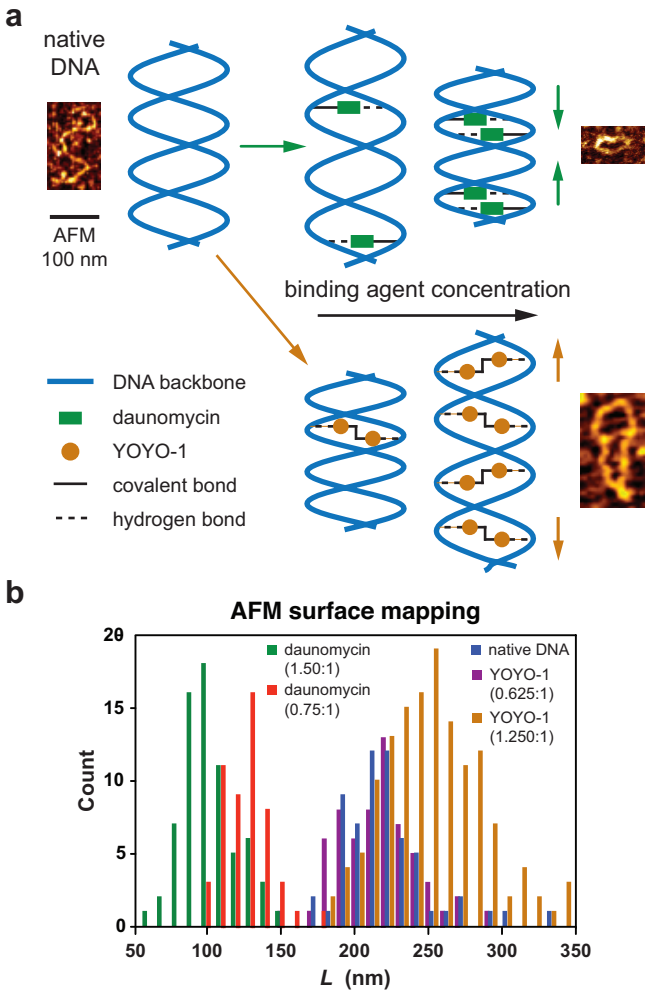

Figure 21 An entropic force microscope quantitatively reveals nano-scale conformation-altering biomolecular interactions.
(a) Illustration of DNA conformational changes associated with daunomycin and YOYO-1 binding measured by resonant entropic transport, shown beside representative AFM images (drawings not to scale, AFM images scaled as indicated). (b) AFM data quantitatively confirm the DNA complex contour length measurements obtained via resonant entropic transport (80 μM DNA base pair concentration complexed with 60 and 120 μM daunomycin, and 50 and 100 μM YOYO-1 (average contour length values are provided in Table 2).

DNA complex* (600 bp dsDNA)		Entropic force microscope (this work)		AFM**
		p **(nm)**	***L*** **(nm)**	***L*** **(nm)**
Native DNA		51 ± 10	229 ± 45	219 ± 29
Daunomycin	0.75:1	49.6± 7.9	134 ± 21	131 ± 16
	1.50:1	55.7 ± 12	100 ± 22	102 ± 18
YOYO-1	0.625:1	52.6 ± 3.4	211 ± 14	213 ± 25
	1.25:1	46.2 ± 5.5	270 ± 32	251 ± 36

Table 2 Persistence and contour lengths of DNA binding complexes obtained via resonant entropic transport.
Contour lengths are compared with corresponding AFM data. DNA concentration in base pairs of 80 μM was used in all cases. Binding agent concentrations are expressed in terms of molecules per DNA base pair. Only contour lengths can be unambiguously determined (mean ± sd, $n \geq 50$).

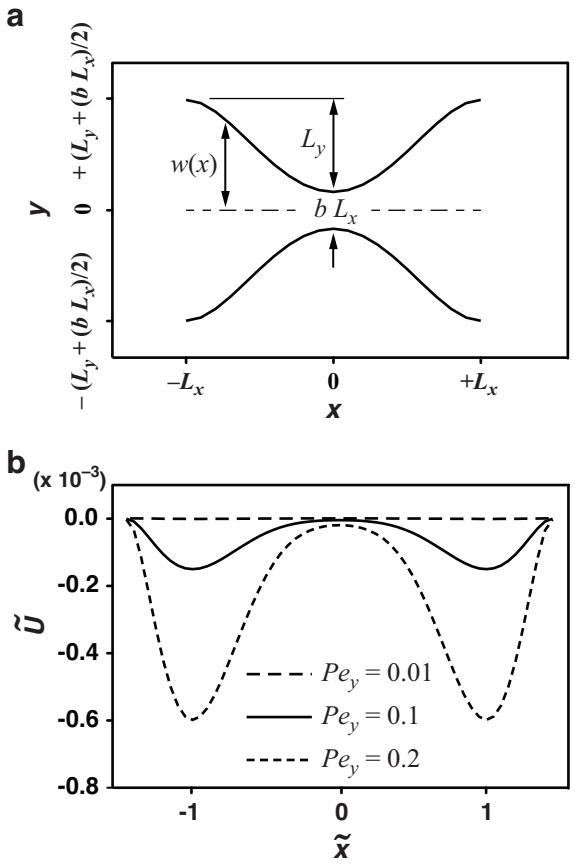

Figure 22 Confinement geometry and energy landscape.
(a) **The microchannel geometry considered incorporates periodically spaced constrictions *w*(*x*) described by Equation 1. In terms of scaled variables, the narrowest and widest regions are defined by *b* and 2*ε* + *b*, respectively (in this study we choose *b* = 0.1 and *ε* = 0.25). A time-periodic driving force F_x is applied along the *x*-direction, and a constant transverse force F_y is imposed in the +*y*-direction. (b) The scaled energy landscape in the absence of the driving force F_x is approximated by a double potential well, where the energy maxima and minima are located at $\tilde{x}_{\max} = 0$ and $\tilde{x}_{\pm\min} = \pm 1$, respectively. Energy landscapes are plotted for three different scaled transverse force conditions expressed in terms of Pe_y. The energy barrier vanishes when the magnitude of the transverse force is small (Pe_y = 0.01, $\tilde{U} \approx 0$), becoming steeper and eventually losing the entropic contribution as the transverse force increases (Burada et al., 2009). We assume Pe_y = 0.1 in all subsequent analysis.**

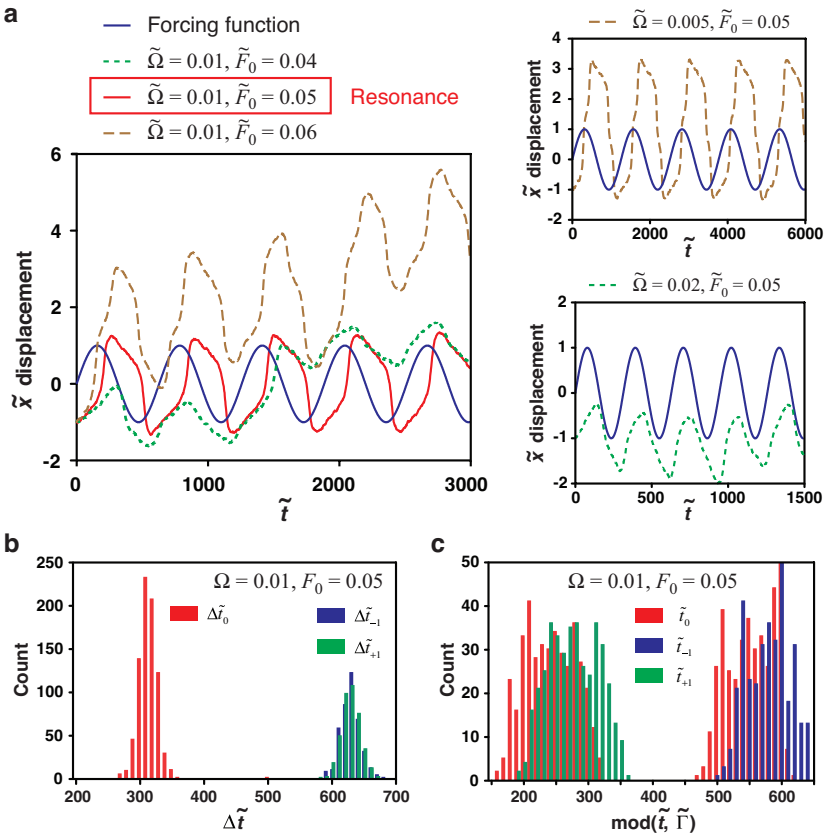

Figure 23 Stochastic resonance in the confining geometry.
(a) SR occurs in the confining microchannel depicted in Figure 1a when $\tilde{F}_0 = 0.05$, $\tilde{\Omega}$ = 0.01, and Pe_y = 0.1. Transport of Brownian particles in response to a periodic driving force (period $\tilde{\Gamma}$ = 628, initial location at $\tilde{x}$ = –1) causes their position oscillate between $\tilde{x}$ = +1 and –1 at a similar period but with a phase lag. The effects of driving force amplitude $\tilde{F}_0$ and frequency $\tilde{\Omega}$ on particle displacement are shown. (b) Statistical distributions of the time interval between passages through successive energy maxima ($\tilde{x} = 0$) and minima ($\tilde{x} = \pm 1$) display synchronization with the driving force period ($\tilde{\Gamma}$ = 628), where $\tilde{t}_0$, $\tilde{t}_{+1}$, and $\tilde{t}_{-1}$ represent the time between successive crossings. The average value of $\tilde{t}_0$ is approximately half of the driving force period due to the fact that each species passes through the energy maximum position twice in single oscillatory period. (c) After dividing the time intervals in (b) by $\tilde{\Gamma}$, a histogram of the remainder is plotted to reveal the corresponding phase lag distributions. Comparison of the averages associated with $\tilde{t}_{-1}$ and $\tilde{t}_{+1}$ with $3\tilde{\Gamma}/4 = 471$ and $\tilde{\Gamma}/4 = 157$ yields a characteristic phase lag of $\tilde{t}_{lag} \approx 100$.

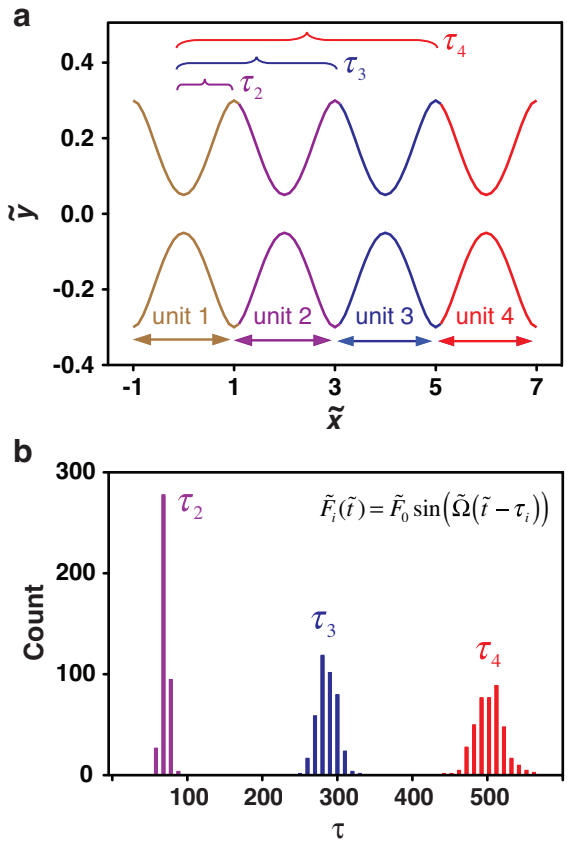

Figure 24 An array of repeated periodic geometries for trapping and separation. (a) A microchannel based on the arrangement depicted in Figure 22 incorporates four repeated constriction units. Energy minima are located at $\tilde{x}$ = –1, 1, 3, 5, 7. Energy maxima are located at $\tilde{x}$ = 0, 2, 4, 6. (b) Phase shifts in the applied driving force τ_i (*i* = 2, 3, 4) are applied to direct confinement within the corresponding constriction units. The distribution of these phase shifts are obtained from Brownian dynamics simulation of a 400 particle ensemble, yielding $\langle\tau_2\rangle \approx \langle\tilde{t}_{\tilde{x}=0} - \tilde{t}_{\tilde{x}=+1}\rangle \sim 100$ and $\langle\tau_3\rangle - \langle\tau_2\rangle \approx \langle\tau_4\rangle - \langle\tau_3\rangle \approx \langle\tilde{t}_{\tilde{x}=+1} - \tilde{t}_{\tilde{x}=-1}\rangle \sim 200$ ($\langle\tau_1\rangle = 0$ by default since particles are initially located at $\tilde{x}$ = 0 in unit 1). Resonant conditions of $\tilde{F}_0 = 0.05$, $\tilde{\Omega}$ = 0.01, and Pe_y = 0.1 are imposed with particles initially located at $\tilde{x}$ = 0.

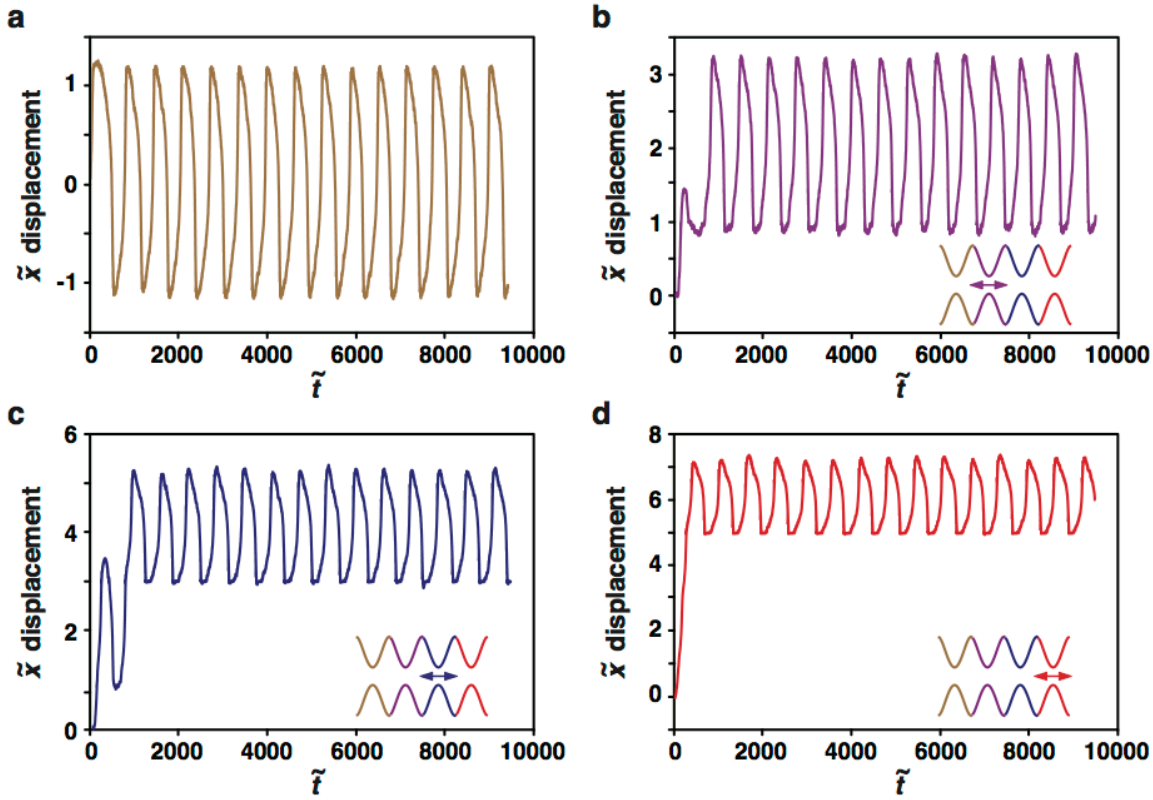

Figure 25 Trapping in a microchannel with periodic confinement.
Individual *x*-displacement trajectories are plotted corresponding to confinement in constriction units (a) 1, (b) 2, (c) 3, and (d) 4 over a time interval of 15 driving force periods (particles are initially located at $\tilde{x} = 0$). The phase value τ_i of the driving force applied in each constriction unit is set to the average values obtained from the distributions in Figure 24-b (the transverse force is held constant in all constriction units). In all cases the periodic driving force $\tilde{F}_0 \sin\left(\tilde{\Omega}\tilde{t}\right)$ is initially uniformly applied throughout the entire geometry. Upon particle entry into an adjacent constriction unit, the periodic force is switched to $\tilde{F}_0 \sin\left(\tilde{\Omega}\left(\tilde{t} - \tau_i\right)\right)$ while the driving force in the previous constriction unit remains unchanged. Resonant conditions of $\tilde{F}_0 = 0.05$, $\tilde{\Omega} = 0.01$, and $Pe_y = 0.1$ are imposed, yielding stable confinement in each constriction unit.

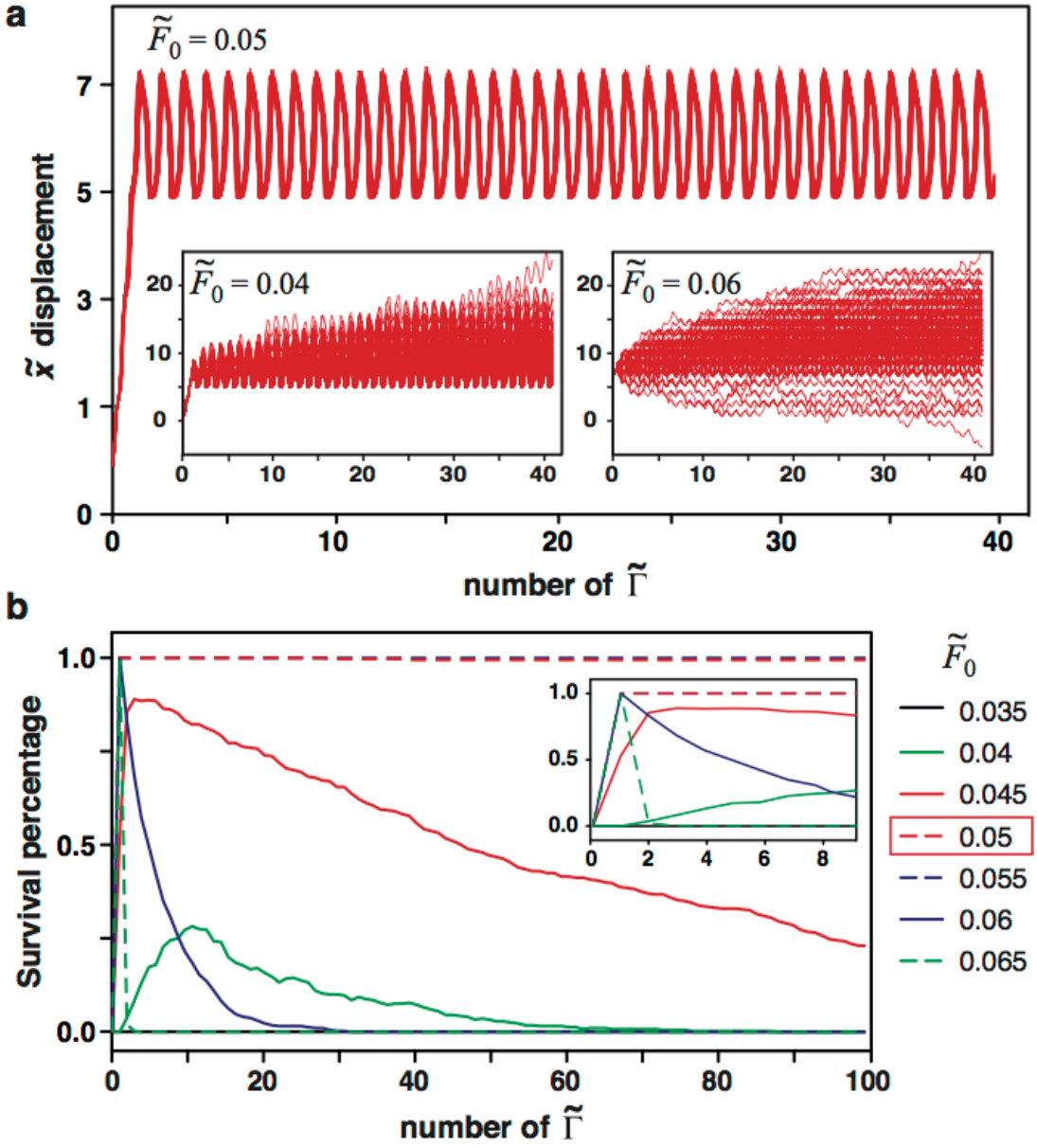
a
$\tilde{F}_0 = 0.05$
$\tilde{F}_0 = 0.04$
$\tilde{F}_0 = 0.06$
$\tilde{x}$ displacement
number of $\tilde{\Gamma}$
b
Survival percentage
number of $\tilde{\Gamma}$
$\tilde{F}_0$
0.035
0.04
0.045
0.05
0.055
0.06
0.065

Figure 26 Influence of the periodically applied driving force amplitude on stability and sensitivity of trapping.
(a) The *x*-displacement of an ensemble of 400 particles is plotted over 40 oscillatory driving force periods under conditions corresponding to Figure 25-d. Stable confinement within the fourth constriction region is evident under resonant conditions ($\tilde{F}_0$ = 0.05). Trapping becomes unstable as $\tilde{F}_0$ deviates from resonance, as evident by trajectories that become broadly dispersed away from the trap location. (b) Data tracking the fraction of the 400 particle ensemble that remain trapped between $\tilde{x}$ = 5 and 7 over a timescale of 100 driving force periods are plotted for different force amplitudes. Under conditions far away from the resonant value of 0.05 (i.e., $\tilde{F}_0$ = 0.06, 0.045 and 0.04), the survival percentage curves initially increase to 1 but then quickly decay back to 0 indicating very weak confinement. Trapping completely breaks down at $\tilde{F}_0$ values that deviate even farther from resonance, as evident by the survival percentage remaining virtually unchanged from 0 (i.e., $\tilde{F}_0$ = 0.065 and 0.035). Remarkably stable trapping is attained at resonance when $\tilde{F}_0$ is close to 0.05, where the survival percentage reaches and maintains a value of 1 throughout the entire simulation time. Conditions of $\tilde{\Omega}$ = 0.01, and Pe_y = 0.1 are imposed in all cases with particles initially located at $\tilde{x}$ = 0.

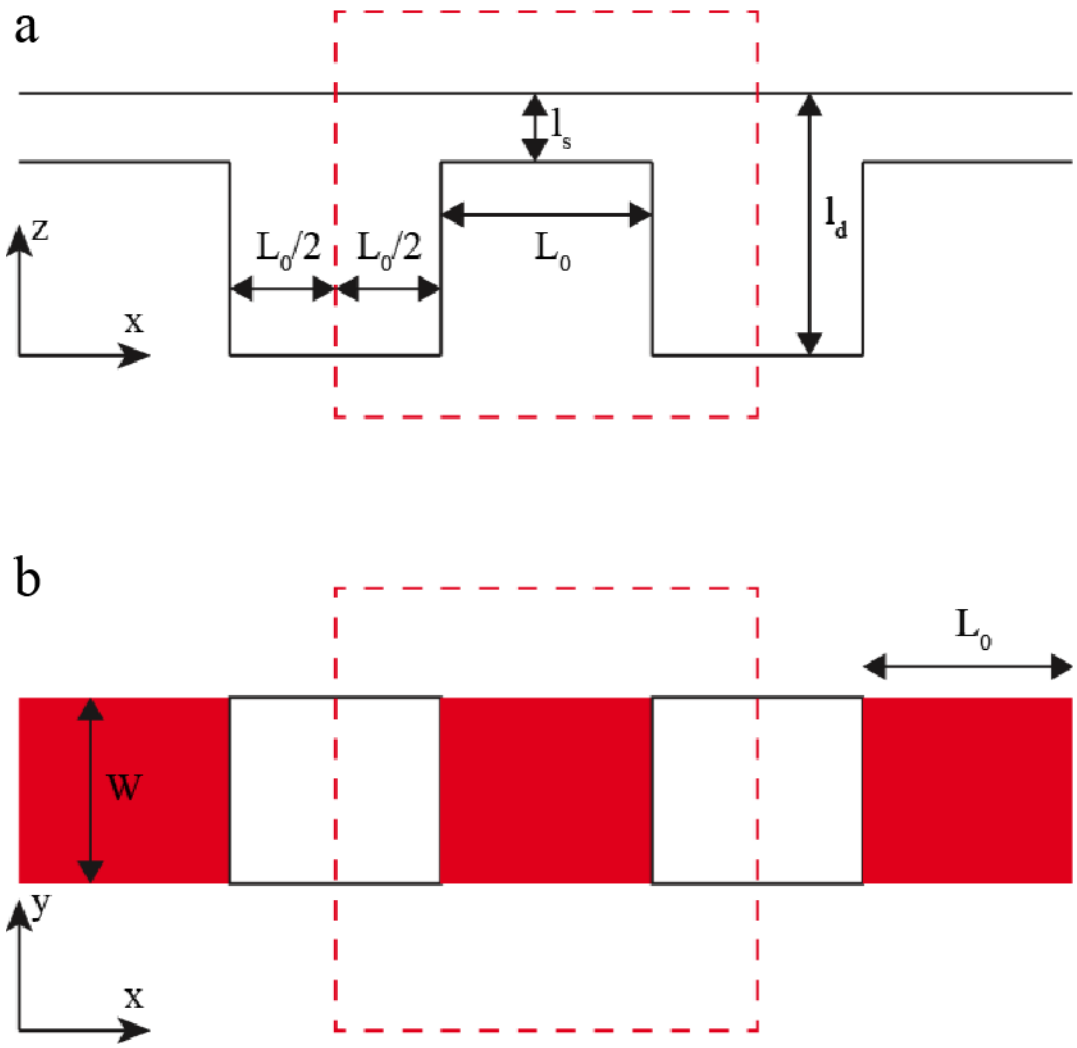

Figure 27 Structure of the nanofilter.
(a) Side view of the nanofilter with alternating nanoslits and deep well. The length of the unit slit and well is both L_0. The depth of slit and well are l_s and l_d, respectively. (b) Top view of the nanofilter with channel width of W. The red dashed rectangle denotes the periodic unit we choose in the simulation. We choose the slit depth l_s = 100 nm, the well depth l_d = 2000 nm, the length L_0 = 2000 nm, channel width W = 2000 nm. These length values are scaled by the Kuhn length (100 nm) of DNA molecule.

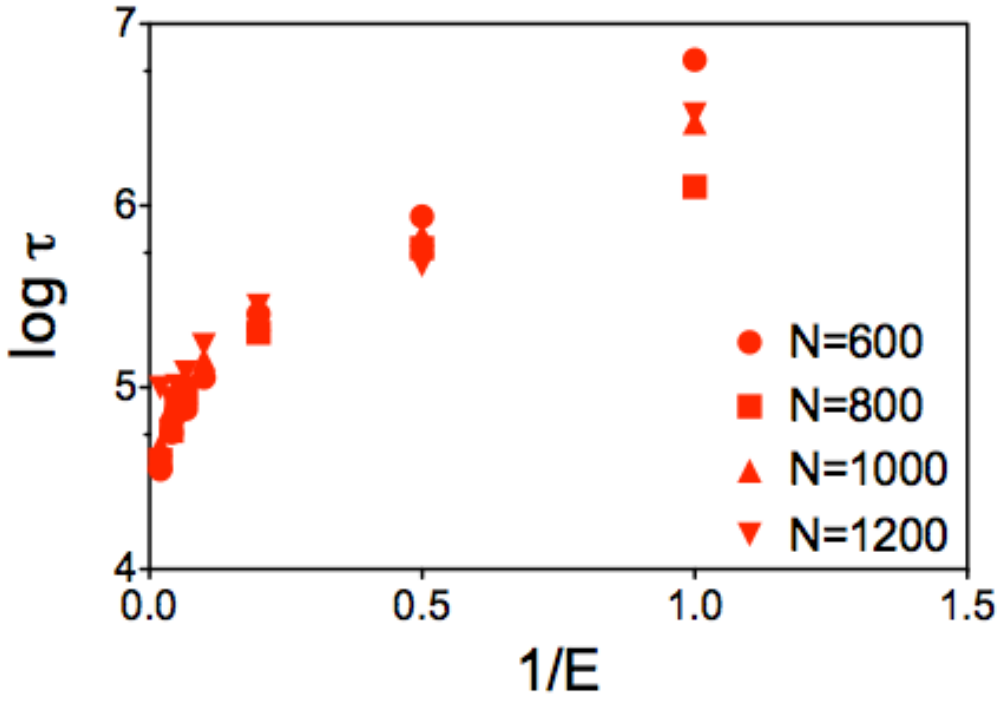

Figure 28 Activation time as a function of the average applied electric field strength.
Four DNA fragments are simulated in the nanoslits driven by electric field ranging from 1V/cm to 50 V/cm. In the high electric field range, the activation time followed previous model as τ_{act}~exp$(1/E)$. However, the scaling behavior changed gradually when the electric field arrives at low electric field range (E<20 V/cm or 1/E>0.05) and can be described by τ_{act}~exp$(1/E^{\alpha})$ with alpha decreasing with lower electric field strength.

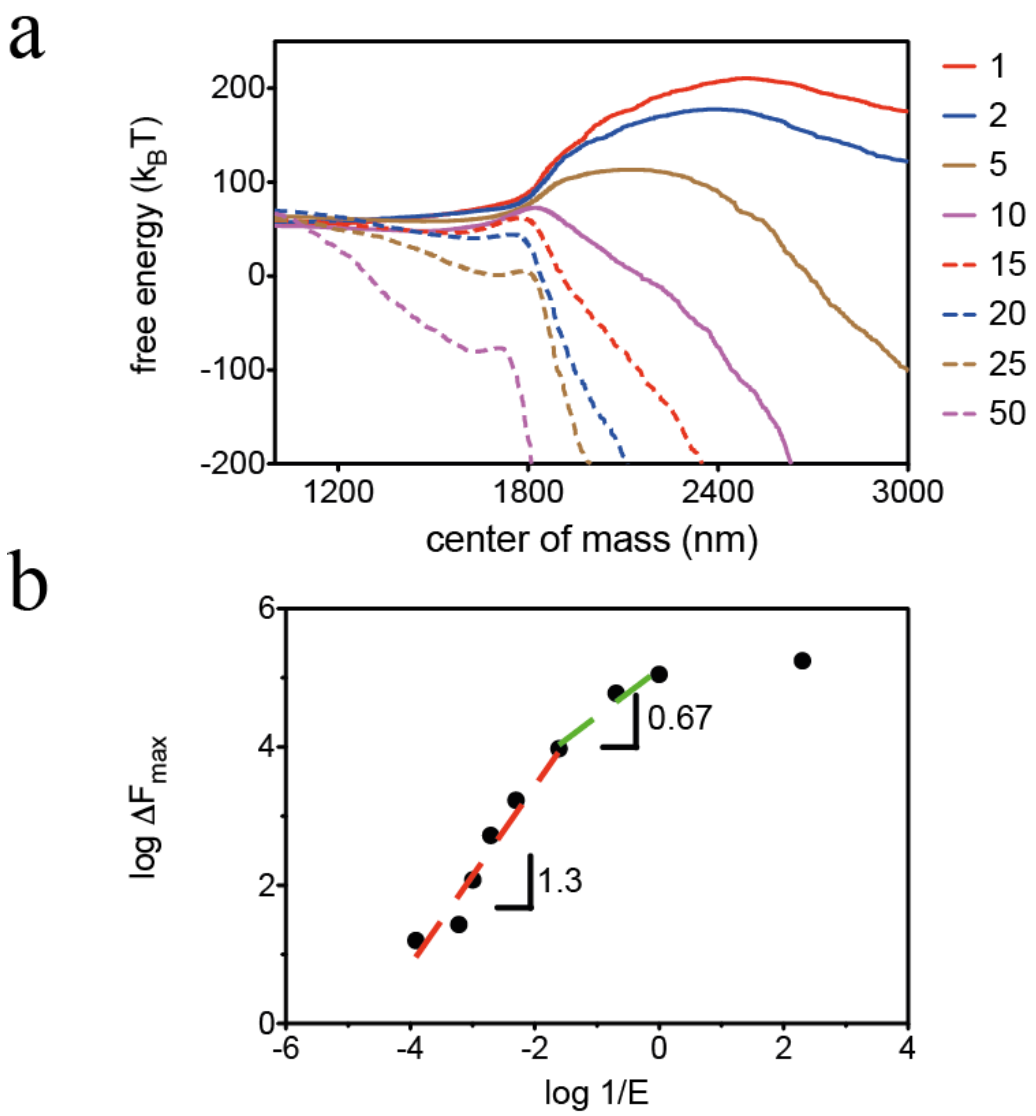

Figure 29 Free energy landscape as DNA migrate into shallow region in channel. (a) **The free energy is plotted against DNA molecules of various displacement of mass center, which could be viewed as the process of single molecule approaching and entering the confining nanoslits. Under all electric field strength (unit: V/cm), the energy trajectories exhibit local maximum indicating the activation energy. Also it is clear that with higher electric field, the DNA molecule experiences the energy barrier at earlier stage and the activation energy is lower than that with lower electric field. (b) The log-log plot of activation energy against the applied electric field strength. The dashed lines and slopes are guiding for changing scaling behavior of activation energy with lower electric field. This scaling trend corresponds with the behavior shown in Figure 28.**

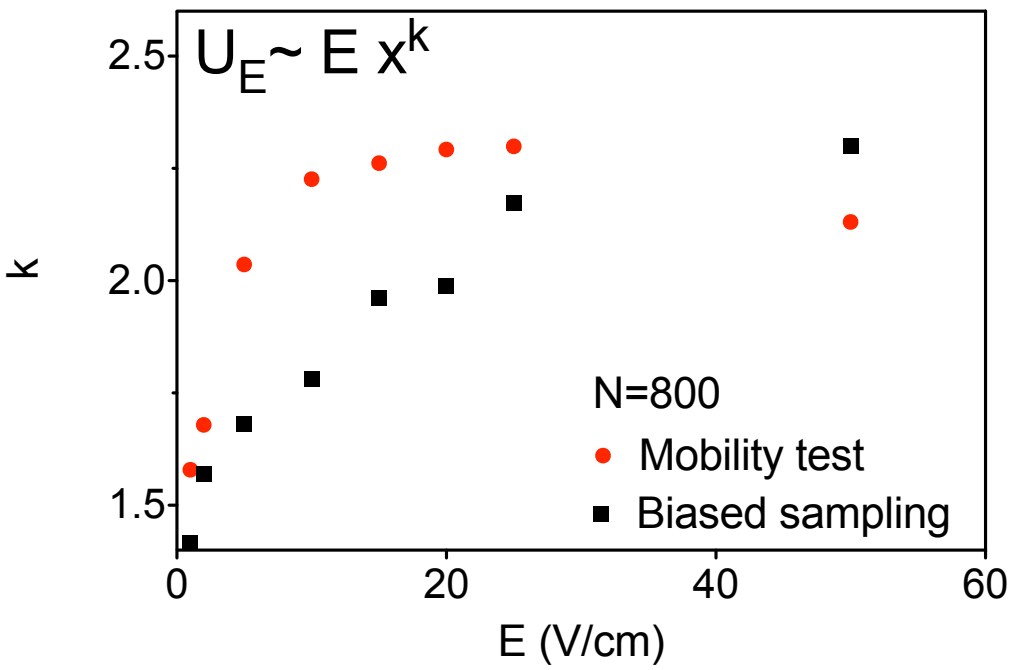

Figure 30 Electrostatic energy shows transition behavior in scaling with the penetration degree.

The scaling power in the relation $U_E \sim E x^k$ is plotted here in different electric field strength. Since the electrostatic energy can be calculated directly from the configuration of DNA molecule, we could get the value from both biased Rosenbluth sampling method (biased sampling, black squares) and the nanoslits migration simulation (mobility test, red dots). Both results confirmed the scaling power k gradually lowers to 1.5 from 2.0 from the fact that DNA molecule is not aligning with the field direction in weak electric field. The DNA sample studied here has 800 segments.

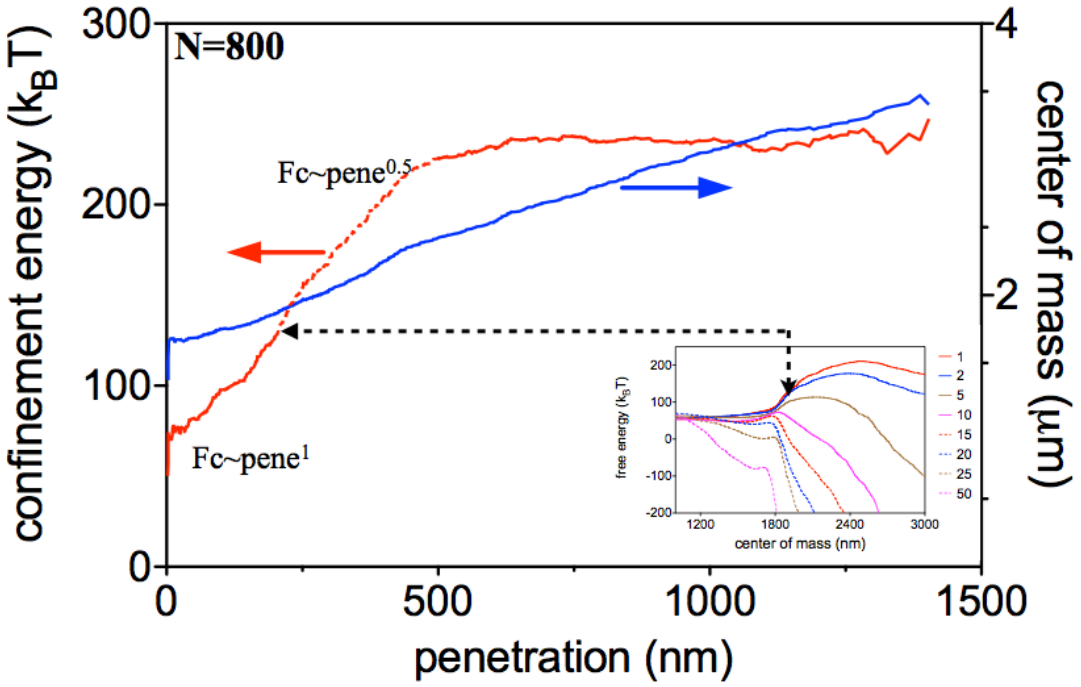

Figure 31 Confinement energy of DNA molecule migrate through nanoslits.
DNA molecule with N=800 segments is studies here, of which the confinement energy shows distinct scaling behaviors in different penetration degrees. During the initial stage of escape when DNA inserts few segments into the slit, confinement energy increases rapidly with the penetration degree (red solid line, linear scaling). As more segments are inside the slit the confinement energy increases with slower pace (red dashed line, power scaling with the power exponent smaller than 1). The two sides arrow with black dashed line points out the position in both the free energy landscape and confinement energy map, before which DNA reaches transition state (maximum free energy) in high electric field strength and after which DNA reaches transition in low electric field.